



HAL
open science

Nonlinear Marangoni convection in circular and elliptical cylinders

Pauline Assemat, Alain Bergeon, Edgar Knobloch

► **To cite this version:**

Pauline Assemat, Alain Bergeon, Edgar Knobloch. Nonlinear Marangoni convection in circular and elliptical cylinders. *Physics of Fluids*, 2007, vol. 19 (n° 10), pp. 1-17. 10.1063/1.2771566. hal-01785165

HAL Id: hal-01785165

<https://hal.science/hal-01785165>

Submitted on 4 May 2018

HAL is a multi-disciplinary open access archive for the deposit and dissemination of scientific research documents, whether they are published or not. The documents may come from teaching and research institutions in France or abroad, or from public or private research centers.

L'archive ouverte pluridisciplinaire **HAL**, est destinée au dépôt et à la diffusion de documents scientifiques de niveau recherche, publiés ou non, émanant des établissements d'enseignement et de recherche français ou étrangers, des laboratoires publics ou privés.



Open Archive TOULOUSE Archive Ouverte (OATAO)

OATAO is an open access repository that collects the work of some Toulouse researchers and makes it freely available over the web where possible.

This is an author's version published in : <http://oatao.univ-toulouse.fr/19850>

Official URL : <https://dx.doi.org/10.1063/1.2771566>

To cite this version :

Assemat, Pauline  and Bergeon, Alain  and Knobloch, Edgar *Nonlinear Marangoni convection in circular and elliptical cylinders.*
(2007) *Physics of Fluids*, vol. 19 (n° 10). pp. 104101. ISSN 1070-6631

Any correspondence concerning this service should be sent to the repository administrator :
tech-oatao@listes-diff.inp-toulouse.fr

Nonlinear Marangoni convection in circular and elliptical cylinders

P. Assemat and A. Bergeon

IMFT UMR CNRS 5502—UPS UFR MIG, 31062 Toulouse Cedex, France

E. Knobloch

Department of Physics, University of California, Berkeley, California 94720, USA

The spatial organization of single-fluid Marangoni convection in vertical cylinders with circular or elliptical horizontal cross section is described. The convection is driven by an imposed heat flux from above through Marangoni stresses at a free but undeformed surface due to temperature-dependent surface tension. The solutions and their stability characteristics are obtained using branch-following techniques together with direct numerical simulations. The changes in the observed patterns with increasing ellipticity are emphasized. In some cases, the deformation of the cylinder results in the presence of oscillations.

[DOI: [10.1063/1.2771566](https://doi.org/10.1063/1.2771566)]

I. INTRODUCTION

Surface tension-driven flows are of importance in a variety of applications, and are a consequence of surface tension inhomogeneities that are either imposed externally or develop spontaneously as a result of an instability. Typical of these is the Marangoni instability that sets in in liquids with a temperature-dependent surface tension once the temperature difference, measured by the Marangoni number, exceeds a critical value. Such flows occur even in the absence of gravity.

Flows of this type are strongly influenced by the absence of reflection symmetry in the midplane of the vessel, a fact responsible for the prevalence of hexagonal structures in large domains. Indeed, the hexagons observed in the original experiment of Bénard are now known to be due to this effect.¹ In smaller domains, the nature of the observed patterns is influenced by the shape of the domain. Experiments by Koschmieder and Prahl² and Ondarçuhu *et al.*³ have focused on Marangoni-driven convection in small aspect ratio square domains, while others have investigated patterns in circular domains;^{2,4-7} to the authors' knowledge, other types of domains have not been investigated. A recent overview of the experimental situation can be found in Ref. 8. In the so-called Rayleigh-Bénard geometry, the multiplicity of states in circular and elliptical domains has been studied by Hof *et al.*⁹ and Meevasana and Ahlers,¹⁰ respectively, and one may expect a similar richness in problems without midplane symmetry of which Marangoni convection is typical.

In the present paper, we use numerical techniques to study large-amplitude convection in circular and nearly circular domains in order to ascertain the effects of the geometry on the transition to steady convection. At first glance this appears straightforward. However, in the process of performing our study we identified a number of unexpected transitions whose origin is of some interest. In addition, we have elucidated some subtle numerical effects that have a surprisingly robust influence on the predicted pattern but are nonetheless artefacts of the grid. These observations may be use-

ful to others attempting Navier-Stokes simulations in containers of circular or nearly circular cross section. Throughout, we use the techniques and language of bifurcation theory to interpret our results.

The paper is organized as follows. In Sec. II, we introduce the basic equations of the study, and review the numerical techniques used to compute the solutions. These include numerical branch following techniques as well as direct numerical simulation. Our results are presented in Sec. III, and interpreted theoretically in Sec. IV. The paper concludes with a summary and a comparison of the results with available experiments.

II. MARANGONI CONVECTION

A. Equations and dimensionless parameters

We study Marangoni convection in a vertical cylinder of elliptical cross section with semimajor axis R and semiminor axis ϵR . Thus when $\epsilon < 1$, the cross section is elongated in the x direction, while for $\epsilon > 1$ it is elongated in the y direction. The case $\epsilon = 1$ corresponds to a circle. In contrast to Ref. 11, a constant normal heat flux $-q > 0$ is applied (in the downward direction) at the free upper surface; finite Biot number effects are neglected. In the following, $A \equiv R/H$ denotes the aspect ratio of the container, where H is its depth. The velocity vanishes along the walls, assumed to be no-slip, and the lateral walls are considered to be adiabatic. The surface tension along the free upper surface varies linearly with the surface temperature: $\sigma(T) = \sigma_0(1 + \gamma_T T)$, where T is the temperature relative to the temperature at the bottom and σ_0 is a constant. We assume that to leading order the free surface remains undeformed by the flow (σ is large) and that the gas in contact with the free surface has no influence. The conditions for stress equilibrium along the free surface are

$$\rho \nu \frac{\partial u}{\partial z} = \sigma_0 \gamma_T \frac{\partial T}{\partial x}, \quad \rho \nu \frac{\partial v}{\partial z} = \sigma_0 \gamma_T \frac{\partial T}{\partial y}, \quad (1)$$

where $\mathbf{u} \equiv (u, v, w)$ is the velocity in (x, y, z) coordinates with the origin in the middle of the lower boundary, ρ is the

density of the fluid, and ν is its kinematic viscosity. This condition is responsible for the onset of convection. The conduction state $\mathbf{u}=\mathbf{0}$, $T=T_c(z)\equiv -qz/\lambda$ is destabilized by temperature fluctuations along the upper surface when the imposed heat flux $-q$ exceeds a critical value as measured by the flux Marangoni number $\text{Ma}\equiv -qH^2\sigma_0\gamma_T/\lambda\rho\nu\kappa$, cf. Ref. 11. Here κ is the thermal diffusivity and $\lambda\equiv C_V\rho\kappa$ is the thermal conductivity. For fluids with $\gamma_T<0$, the above formulation remains valid provided the sign of q is reversed, i.e., provided the surface is cooled instead of being heated.

In the following, distance, time, temperature, and velocity are nondimensionalized using H , H^2/ν , $\Delta T\equiv -qH/\lambda$, and $\text{Ma}\nu/H$, respectively. In zero gravity, the dimensionless equations for \mathbf{u} , p , and T are

$$\partial_t\mathbf{u} = -\text{Ma}(\mathbf{u}\cdot\nabla)\mathbf{u} - \nabla p + \nabla^2\mathbf{u}, \quad \nabla\cdot\mathbf{u} = 0, \quad (2)$$

$$\partial_t T = -\text{Ma}(\mathbf{u}\cdot\nabla)T + \text{Pr}^{-1}\nabla^2 T, \quad (3)$$

where \mathbf{u} , p , T , x , y , z , and t now refer to dimensionless variables, and $\text{Pr}\equiv \nu/\kappa$ is the Prandtl number. The boundary conditions along the free surface ($z=1$) are

$$\partial_z u - \text{Pr}^{-1}\partial_x T = \partial_z v - \text{Pr}^{-1}\partial_y T = w = \partial_z T - 1 = 0, \quad (4)$$

while those along the bottom ($z=0$) are $u=v=w=T=0$. Along the lateral walls we have $u=v=w=\partial_n T=0$, where n is the coordinate normal to the wall. Consequently, the pure conduction state $[\mathbf{u}=\mathbf{0}, T(z)=z]$ is a solution of the problem for any Marangoni number Ma . In this paper, we focus on containers with a relatively small aspect ratio ($A\approx 1$) and examine the transitions that take place with increasing elliptical deformation of the container.

B. Numerical method

Our primary purpose is to apply numerical branch-following algorithms in three spatial dimensions in order to elucidate the complete bifurcation structure of Marangoni convection for aspect ratios for which the solution multiplicity is still relatively small. This is the case for the aspect ratios we use in this paper. The branch-following method used in our case can be implemented by combining an existing first-order time-stepping code employing projection methods for time integration¹² with an iterative (Newton method) wraparound to compute the fixed points of the system, as suggested by Mamun and Tuckerman.¹³ This technique is used here to calculate both linear and nonlinear solutions of the problem as described in Ref. 14.

We use a spectral element method for the space discretization of the equations in conservation form. The computational domain is partitioned into N_e nonoverlapping elements Ω_l ($1\leq l\leq N_e$) (Fig. 1). The reference coordinate system $\hat{\mathbf{x}}\equiv(\hat{x},\hat{y},\hat{z})$ defines a cubic domain $\hat{\Omega}=[-1,1]^3$. Data are expressed as tensor products of Lagrange polynomials based on the Gauss-Lobatto-Legendre (GLL) quadrature points. Functions in the system coordinates $\mathbf{x}\equiv(x,y,z)$ are of the form

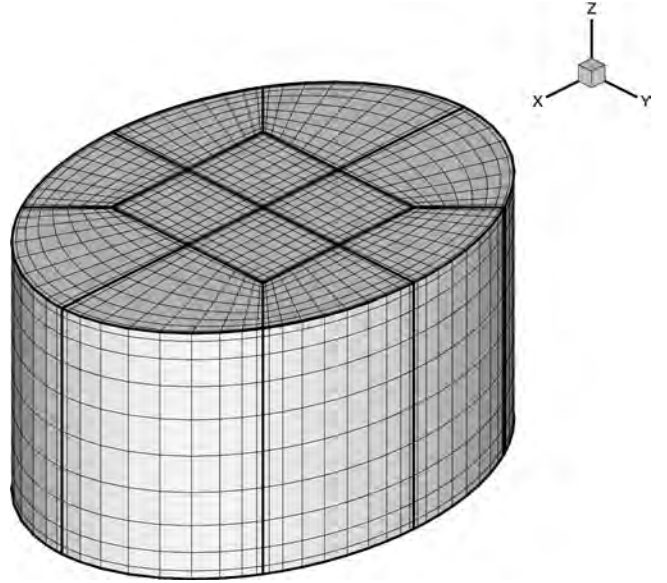


FIG. 1. View of the grid in an elliptical geometry. The grid has $N_e=12$ macro-elements. Spatial resolution in each element is $n_x=n_y=n_z=10$, where n_x , n_y , and n_z are, respectively, the polynomial degrees of the interpolant in the x , y , and z directions.

$$u[\mathbf{x}^l(\hat{\mathbf{x}})] = \sum_{i=0}^{n_x} \sum_{j=0}^{n_y} \sum_{k=0}^{n_z} u_{ijk}^l h_i^{n_x}(\hat{x}) h_j^{n_y}(\hat{y}) h_k^{n_z}(\hat{z}), \quad (5)$$

where u_{ijk}^l are the nodal basis coefficients, $h_i^{n_x}(\hat{x})$ [respectively, $h_j^{n_y}(\hat{y})$ and $h_k^{n_z}(\hat{z})$] are Lagrange polynomials of degree n_x (respectively, n_y and n_z) based on the GLL quadrature points, and $\mathbf{x}^l(\hat{\mathbf{x}})=(x^l(\hat{\mathbf{x}}), y^l(\hat{\mathbf{x}}), z^l(\hat{\mathbf{x}}))$ is the coordinate mapping from the reference domain $\hat{\Omega}$ to Ω_l .

In the projection scheme used for the momentum equation, the linear terms are integrated implicitly and the nonlinear terms explicitly. The first-order version of the scheme reads

$$\Delta t^{-1}(\mathbf{u}^{(n+1)} - \mathbf{u}^{(n)}) = -\text{Ma}(\mathbf{u}^{(n)}\cdot\nabla)\mathbf{u}^{(n)} - \nabla p^{(n+1)} + \nabla^2\mathbf{u}^{(n+1)}, \quad (6)$$

where $\mathbf{u}^{(n)}$ refers to the velocity field at time $t_n\equiv n\Delta t$. Each time step is subdivided into three substeps. After the computation of the nonlinear terms (the first substep), a Poisson problem is formulated for the pressure using the boundary conditions proposed in Ref. 12. This Poisson problem (second substep) as well as the Helmholtz problems for the velocity components that constitute the final implicit substep of the scheme are solved using a variational formulation. Since a similar treatment is done for the heat equation, each time step involves the inversion of four Helmholtz problems (one for the temperature T and one for each velocity component) and one Poisson problem (for the pressure). The inversions are performed using a Schur method taking full advantage of the tensorization in the z direction. Throughout the paper, we use $N_e=12$ spectral elements.

To check the accuracy of the method, we compare our results with Refs. 15 and 16. A direct comparison is difficult as the results of Refs. 15 and 16 are presented graphically. To check the accuracy of the critical Marangoni number, i.e., the

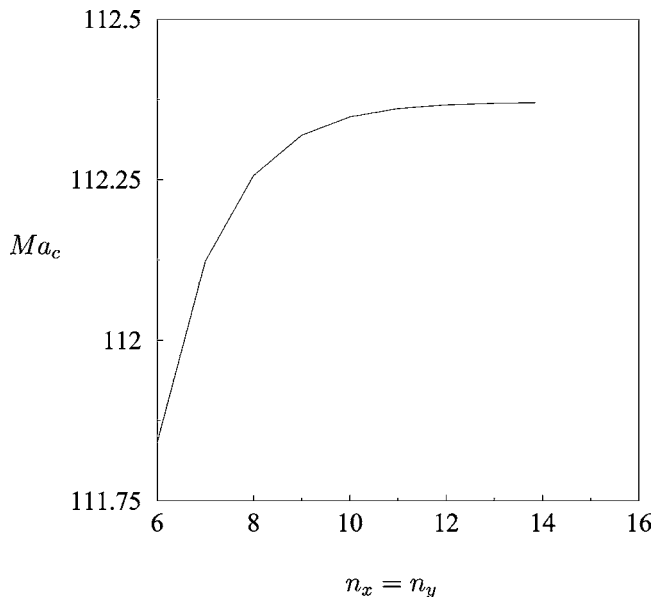


FIG. 2. Evolution of the critical Marangoni number for the $m=1$ mode with the grid spacing $n_x=n_y$, when $\text{Pr}=1$, $A=1.5$, and $n_z=10$ (cf. Fig. 11).

primary bifurcation point for different aspect ratios, we have therefore employed three methods. The first uses Arnoldi's method¹³ to calculate the largest eigenvalues of large linear systems. For the linear stability problem of the conduction state, this method yields the largest eigenvalues at discrete values of Ma . The critical Marangoni number corresponds to a zero maximum eigenvalue. In an $A=1$ container with $n_x \times n_y \times n_z = 10 \times 10 \times 10$ interpolation yields $\text{Ma}_c = 109.035$.

The second method solves the system $\mathbf{DF}(\text{Ma})\mathbf{h}=\mathbf{0}$, where \mathbf{DF} denotes the linearized version of the discretized equations around the conduction state, and $\mathbf{h} \equiv (u_{ijk}^l, v_{ijk}^l, w_{ijk}^l, T_{ijk}^l)$, $0 \leq i \leq n_x$, $0 \leq j \leq n_y$, $0 \leq k \leq n_z$, $1 \leq l \leq N_e$, are the values of the three velocity components and temperature at the grid points. This is a nonlinear system as both \mathbf{h} and Ma are unknowns. This problem is solved using a Newton method as described in Ref. 14. Consequently, no eigenvalue computation is involved. The method converges well as the number of grid points (Fig. 2 and Table I) is increased. The third method uses an extrapolation of fully nonlinear solutions to zero amplitude (Fig. 3). For $A=1$ with $n_x \times n_y \times n_z = 10 \times 10 \times 10$, the extrapolation yields $\text{Ma}_c = 109.029$. Thus all three methods are in excellent agreement with each other and with the values obtained in the previously cited papers.

Our numerical method keeps track of the unstable eigenvalues along each solution branch. For bifurcations that break the circular symmetry of the container, these eigenval-

TABLE I. Critical Marangoni number Ma_c for different grids and aspect ratios.

| $n_x \times n_y \times n_z$ | $6 \times 6 \times 10$ | $10 \times 10 \times 10$ | $14 \times 14 \times 10$ | $10 \times 10 \times 14$ |
|-----------------------------|------------------------|--------------------------|--------------------------|--------------------------|
| $m=1, A=1$ | 109.0726 | 109.0286 | 109.0283 | 108.9071 |
| $m=0, A=2.1$ | 84.1408 | 84.0812 | 84.0810 | 84.0818 |
| $m=1, A=2.8$ | 82.9163 | 82.7896 | 82.7832 | 82.7871 |

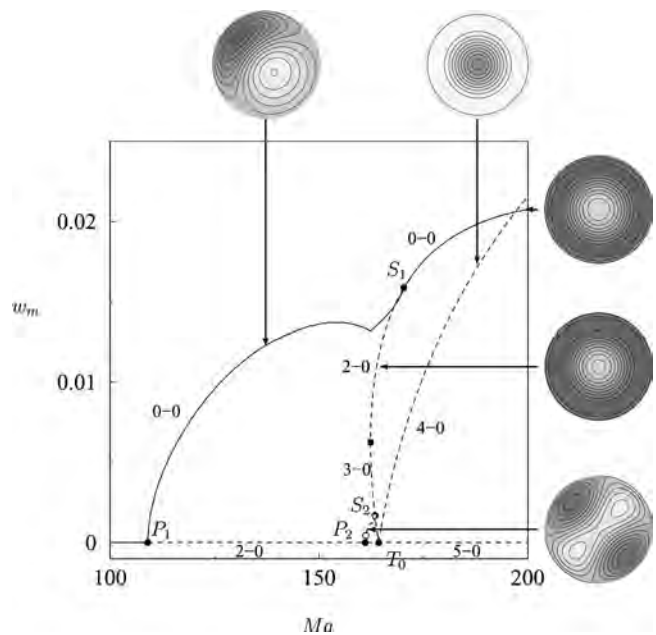


FIG. 3. Bifurcation diagram showing the maximum of the vertical velocity w_m as a function of the Marangoni number Ma . Snapshots show isovalues of the vertical velocity in the midplane of the cylinder. The orientation of the $m \neq 0$ states is nominally arbitrary. Parameters are $\epsilon=1$, $A=1$, and $\text{Pr}=1$. Resolution is $N_e=12$, $n_x=n_y=n_z=10$.

ues are doubled. Thus it is important to characterize all solutions by their symmetry; this symmetry typically reflects the symmetry of the unstable eigenfunction responsible for the instability, although, as we shall see, this is not always the case.

In the following section, we will see how the multiplicity of the eigenvalues is reduced as the cylinder cross section becomes elliptical. We compute numerically the bifurcation diagrams for both $O(2)$ -symmetric (circular) and D_2 -symmetric (elliptical) cross sections with our continuation method. All primary bifurcations are steady-state bifurcations since the eigenvalues of the linear stability problem are necessarily real.^{11,17} Periodically we calculate the leading eigenvalues of the linearized system (around the nonlinear state) using an adaptation of Arnoldi's method described in Ref. 13. When the number of positive eigenvalues changes, indicating a bifurcation, the method determines the parameter interval in which the bifurcation occurs together with the associated eigenvector. The latter is used to initiate branch switching. Secondary bifurcation points are located from the intersection of pairs of nonlinear branches with different numbers of unstable eigenvalues, and for the aspect ratios used the results using a $10 \times 10 \times 10$ grid agree well with the results of direct numerical integration. All calculations use $\text{Pr}=1$ since the value of Pr has no effect on the primary bifurcations.

III. RESULTS

In this section, we describe the results for containers of both circular and elliptical cross section and different aspect ratios. The results are presented in the form of bifurcation diagrams, and use solid circles to indicate primary bifurca-

tions and secondary pitchfork bifurcations, while solid squares indicate saddle-node bifurcations, open circles indicate (secondary) Hopf bifurcations, and open triangles indicate collisions of a pair of complex eigenvalues on the positive real axis; the latter, of course, does not correspond to a bifurcation. Primary bifurcations are labeled using the notation P_m , T_m to indicate pitchfork (P) and transcritical (T) bifurcations to modes with azimuthal wavenumber m . In the following, we refer to eigenvalues with a negative (positive) real part as stable (unstable) eigenvalues. Stability of each branch is indicated using the notation $n-p$, where n is the number of unstable real eigenvalues and p is the number of pairs of unstable complex eigenvalues. Thus the number of unstable eigenvalues is $n+2p$. In the figures, we use solid (dashed) lines to indicate linearly stable (unstable) solutions. We do not follow branches of time-periodic states. In many of the bifurcation diagrams, we include snapshots of the flow showing the vertical velocity w at midheight, with dark (light) shading indicating $w < 0$ ($w > 0$).

Throughout the description that follows, we refer to states that are reflection-symmetric about $x=0$ ($y=0$) as κ_y -symmetric (κ_x -symmetric).

A. Aspect ratio $A=1$

We begin with aspect ratio $A=1$ and describe the changes that occur in the solutions of the nonlinear problem as the ellipticity ϵ is reduced from $\epsilon=1$. The diameter in the x direction is kept equal to 1 throughout. We refer to Ref. 18 for a similar study of square and nearly square containers. Figure 3 shows the bifurcation diagram for the circular container. The figure displays the evolution with the Marangoni number of the maximum w_m of the absolute value of the vertical component of the velocity at the Gauss-Lobatto-Legendre nodes.¹⁹ The value $w_m=0$ corresponds to the conduction state. Branches with $w_m \neq 0$ are characterized by the azimuthal wavenumber m of the state, indicated in the label of the corresponding primary bifurcation.

Figure 3 shows that the conduction state is stable up to $\text{Ma}_{P_1}=109.03$. At this value of the Marangoni number the conduction state undergoes a symmetry-breaking bifurcation that produces a branch of states with azimuthal wavenumber $m=1$. As a result, the eigenvalue that passes through zero at Ma_{P_1} is doubled, and the resulting bifurcation is a pitchfork of revolution. The figure reveals that this bifurcation is supercritical, and the resulting solutions are therefore stable (modulo a zero eigenvalue associated with spatial rotations of the pattern). We note, however, that the solutions are not invariant under a change in sign of w_m . This is a consequence of the different boundary conditions applied at the top and bottom of the container.

The second primary bifurcation occurs at $\text{Ma}_{P_2}=161.1$ and is also a supercritical pitchfork of revolution, this time producing a branch of $m=2$ solutions (Fig. 4). These solutions inherit the instability of the conduction state in $\text{Ma}_{P_1} < \text{Ma} < \text{Ma}_{P_2}$ and hence are doubly unstable. Moreover, like the $m=1$ solutions, the $m=2$ solutions are not invariant under change of sign.

The final primary bifurcation we discuss occurs at

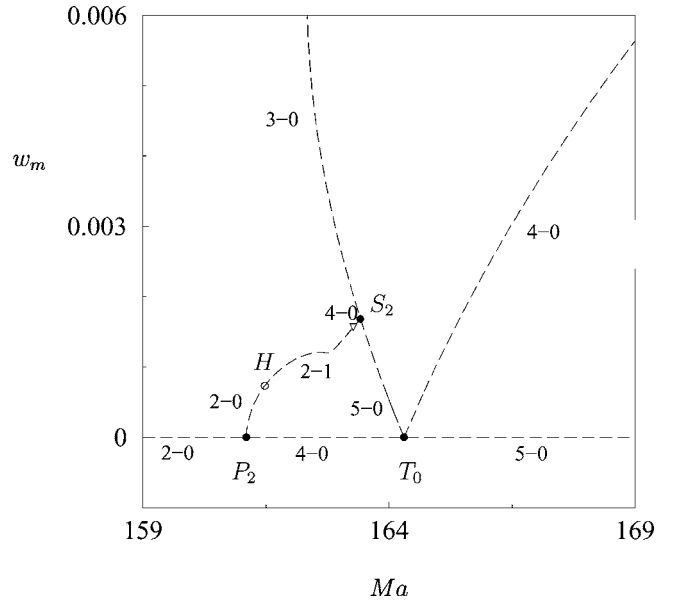


FIG. 4. Detail of Fig. 3.

$\text{Ma}_{T_0}=164.2$, and corresponds to a transcritical bifurcation to an $m=0$ state, i.e., to an axisymmetric state. Since this bifurcation is unaffected by the $O(2)$ symmetry of the system, only one eigenvalue passes through zero at Ma_{T_0} , with the supercritical branch inheriting the four unstable eigenvalues of the conduction state, while the subcritical part is five times unstable.

Figure 3 shows how these branches interact in the nonlinear regime. The $m=1$ branch terminates on the $m=0$ branch above a saddle-node bifurcation ($\text{Ma}=162.34$, indicated by a solid square) at a point labeled S_1 characterized by a double zero eigenvalue. The bifurcation at S_1 is mathematically identical to that at P_1 : the $m=0$ state loses stability with decreasing Ma at a pitchfork of revolution at S_1 , and is therefore doubly unstable below S_1 (and above the saddle node). The prominent kink in the $m=1$ branch just prior to S_1 is a consequence of increasing importance of the $m=0$ contribution, which shifts the local maximum in w to a new location, and is not the result of a bifurcation. The figure shows that the $m=2$ branch also terminates on the $m=0$ branch, but this time below the saddle node, at a point labeled S_2 . Once again, at this point there is a double zero eigenvalue. We find that above S_2 (and below the saddle node) the $m=0$ branch is three times unstable; it follows that the $m=2$ branch near S_2 must be four times unstable, and hence that the $m=2$ branch must undergo a Hopf bifurcation between P_2 and S_2 , a conclusion that has been verified numerically (Fig. 4). Indeed, the complex unstable eigenvalues created at the Hopf bifurcation collide on the positive real axis with increasing Ma , before one of them reaches zero at S_2 ; the other zero eigenvalue at S_2 comes from rotations of the $m=2$ states. The number of unstable eigenvalues along each solution branch is indicated in the figure, and is consistent with the above theoretical expectation. Since the Hopf bifurcation preserves the symmetry of the $m=2$ state, the resulting (unstable) oscillations are standing waves, and likely disappear in a global bifurcation involving the $m=0$ state.

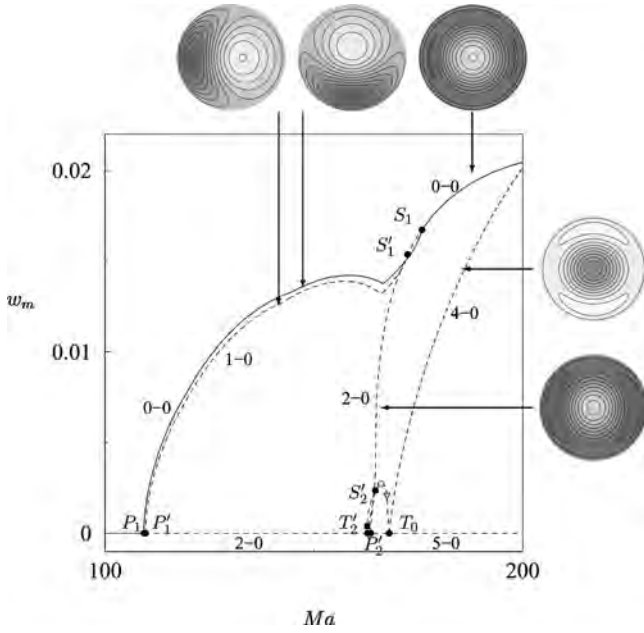


FIG. 5. Bifurcation diagram showing the maximum of the vertical velocity w_m as a function of the Marangoni number Ma . Snapshots show isovals of the vertical velocity in the midplane of the cylinder. Parameters are $\epsilon=0.98$, $A=1$, and $Pr=1$. Resolution is $N_e=12$, $n_x=n_y=n_z=10$.

It will have been noticed that the $m=1$ and $m=2$ states are both oriented at 45° to the x axis. This is a consequence of the structure of the numerical grid used to compute the solutions (Fig. 1). The grid used is not rotationally invariant but has in fact residual D_4 symmetry. This symmetry group, the symmetry of a square, is generated by two reflections, κ_x in the x axis and Π_{xy} in the line $x=y$. As discussed below, the small perturbations due to the structure of the grid split each of the $m=1$ and $m=2$ branches into a pair of branches, one consisting of states with κ_x symmetry and the other of Π -symmetric states; each branch is produced in a standard pitchfork bifurcation that come in in close succession. It turns out that in each case the grid selects the Π -symmetric state as the first state that sets in. A similar observation applies to the termination point S_2 , which is also split by the grid. Both $m=2$ branches undergo the Hopf bifurcation to standing oscillations prior to their termination on the $m=0$ branch.

We now turn to a discussion of the corresponding results for a slightly elliptical container, characterized by $\epsilon=0.98$. Although the resulting ellipticity is small, this value is still sufficiently far from $\epsilon=1$ that the ellipticity effects ought to dominate the symmetry-breaking effects due to the grid. It should be mentioned that the elliptical deformation of the container cross section changes the symmetry of the problem to D_2 , the symmetry group of a rectangle, a smaller symmetry group than D_4 . The former is generated by the two reflections κ_x and κ_y , and in contrast to κ_x and Π these commute. Figure 5 shows that this change in the symmetry of the problem results in a substantial change in the bifurcation diagram. Since the primary bifurcations can only lead to κ_x - and κ_y -symmetric states, the multiple bifurcations at P_1 and P_2 are strongly affected. Figure 5 shows that P_1 is split, with the

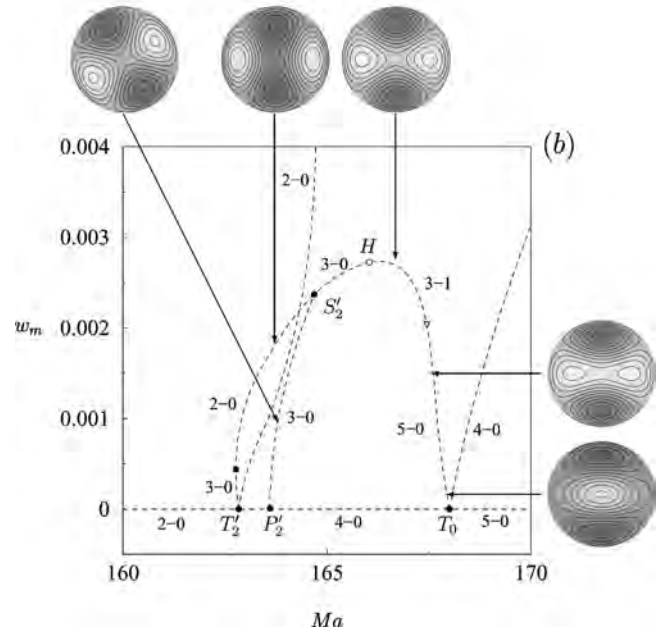
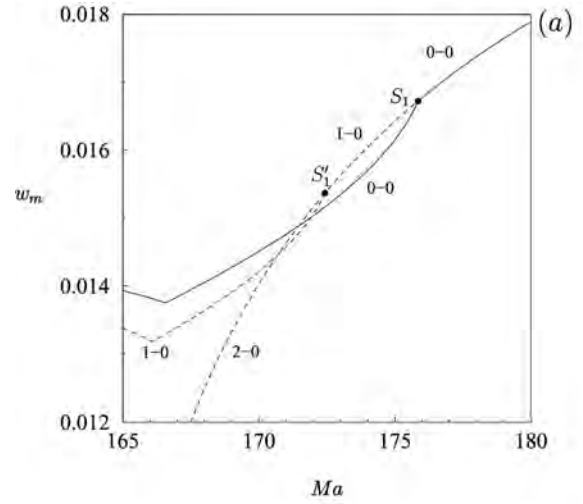


FIG. 6. (a),(b) Detail of Fig. 5.

κ_y -symmetric states coming in first, followed by the κ_x -symmetric states; the former are stable, while the latter are once unstable. The bifurcation at P_2 is also split, resulting in a transcritical bifurcation to D_2 -symmetric states and a pitchfork to Π -like states [Fig. 6(b)]. In fact, these states, which come in at the point labeled P_2' , have exact Π symmetry at zero amplitude, but with increasing amplitude their plane of symmetry rotates monotonically, reaching 45° by the time the branch terminates at S_2' . The reason for this unexpected behavior will be explained below. Figure 6(b) also shows that one of the transcritical branches created in the breakup of P_2 connects to the large-amplitude axisymmetric states at S_1' , while the other undergoes a saddle-node bifurcation before connecting to the second transcritical bifurcation T_0 ; the latter is merely the (slightly perturbed) transcritical bifurcation T_0 present in the $O(2)$ -symmetric case; the same notation is therefore used to refer to it. This connection contains a Hopf bifurcation to standing oscillations

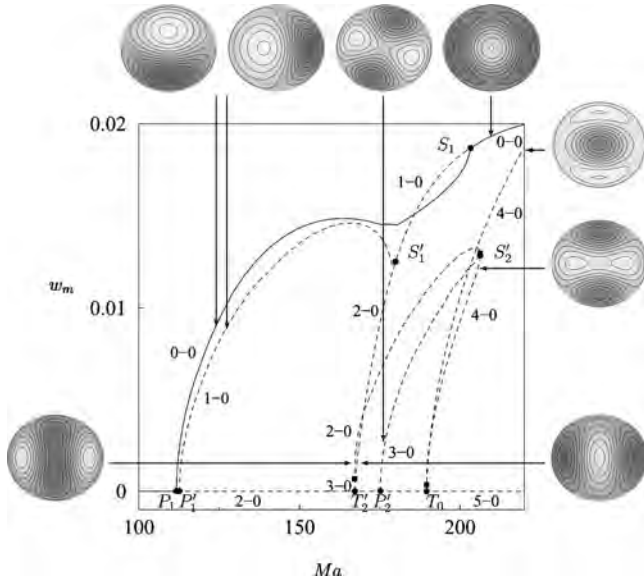


FIG. 7. Bifurcation diagram showing the maximum of the vertical velocity w_m as a function of the Marangoni number Ma . Snapshots show isovals of the vertical velocity in the midplane of the cylinder. Parameters are $\epsilon=0.90$, $A=1$, and $Pr=1$. Resolution is $N_e=12$, $n_x=n_y=n_z=10$.

with D_2 symmetry, but the resulting oscillations are necessarily unstable. It should be noted that this bifurcation is present *after* S'_2 ; for ϵ closer to $\epsilon=1$, the order of these bifurcations is reversed, while a second Hopf bifurcation is present on the branch of Π -like states connecting P'_2 to S'_2 . Finally, the forced symmetry breaking to D_2 also splits the termination point S_1 (Fig. 3), with the result that the κ_y -symmetric states transfer stability to the D_2 -symmetric states arising from the axisymmetric states [at S_1 in Fig. 6(a)], while the unstable branch of κ_x -symmetric states terminates on the D_2 -symmetric states just below [at S'_1 in Fig. 6(a)]. Once again the number of unstable eigenvalues along each branch is indicated in the figure.

Figure 7 shows the corresponding results for $\epsilon=0.90$, i.e., for larger ellipticity. The broad features of the bifurcation diagram are similar. The main difference involves the branch of D_2 -symmetric states connecting the two primary transcritical bifurcations. Figure 7 shows that this branch now undergoes an additional saddle-node bifurcation on the right; the termination point S'_2 of the Π -like states falls on the part of the D_2 branch just below this saddle node. Moreover, the secondary Hopf bifurcation is now absent; this bifurcation collides with the saddle-node bifurcation with increasing ellipticity, and disappears via the so-called Takens-Bogdanov bifurcation. This bifurcation is then followed by a second (and different) codimension-2 bifurcation at which S'_2 passes through the saddle node.

Figure 8 shows the corresponding results for $\epsilon=0.75$. For this value of ϵ the order of the primary bifurcations is reversed. The reason for this is indicated in Fig. 9, which shows the linear stability thresholds for $m=1$ modes in the (ϵ, Ma) plane. The figure shows that outside the region $0.8 < \epsilon \leq 1$, the mode that first sets in is the mode with κ_x symmetry; the first unstable mode is κ_y -symmetric only in the range $0.8 < \epsilon \leq 1$. Because of the mode exchange that

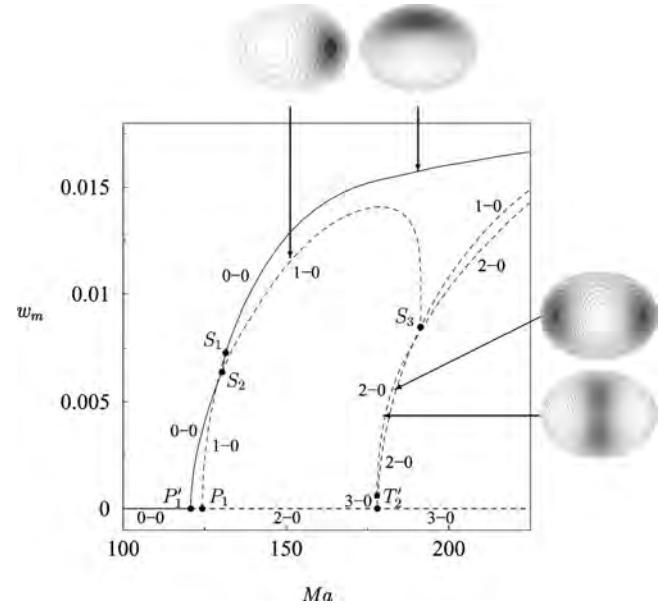


FIG. 8. Bifurcation diagram showing the maximum of the vertical velocity w_m as a function of the Marangoni number Ma . Snapshots show isovals of the vertical velocity in the midplane of the cylinder. Parameters are $\epsilon=0.75$, $A=1$, and $Pr=1$. Resolution is $N_e=12$, $n_x=n_y=n_z=10$.

takes place near $\epsilon=0.8$, the κ_x -symmetric states must transfer their stability to the κ_y -symmetric states in the nonlinear regime. Figure 10 shows that this transfer of stability occurs via a stable branch of mixed states, i.e., a branch of states with no symmetry. As a result, the stable large-amplitude states, away from the primary bifurcation, continue to be the κ_y -symmetric states.

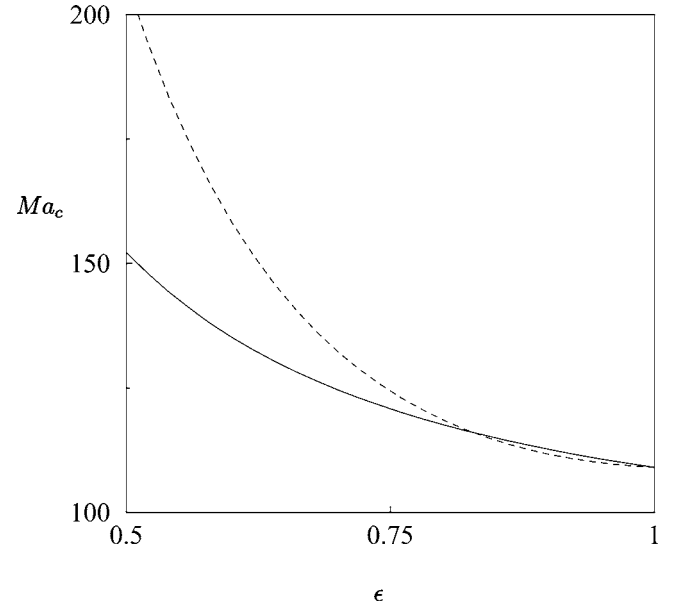


FIG. 9. Critical Marangoni number Ma_c as a function of the ellipticity ϵ . The azimuthal wavenumber is $m=1$. Parameters are $A=1$ and $Pr=1$. The primary bifurcation with $\epsilon=1$ is split into two successive bifurcations: solid line indicates κ_x -symmetric states, dashed line κ_y -symmetric states. Resolution is $N_e=12$, $n_x=n_y=n_z=10$.

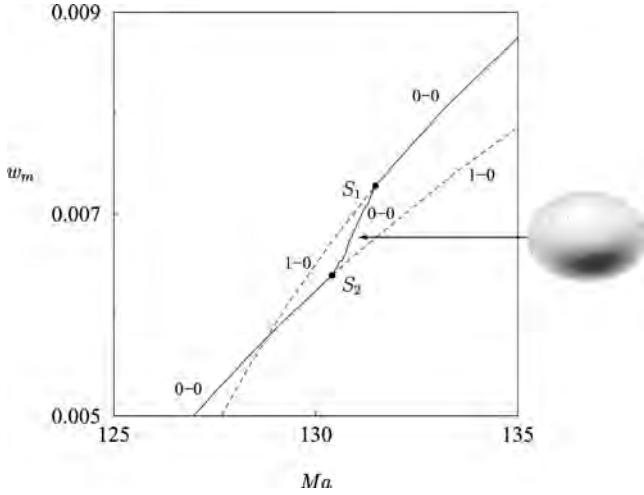


FIG. 10. Closer view of Fig. 8 showing exchange of stability between κ_x - and κ_y -symmetric states via a stable branch of nonsymmetric states.

B. Aspect ratio $A=1.5$

Figure 11 shows the linear stability thresholds for $A=1.5$, again as a function of ϵ . The primary instability is always to $m=0$ -like states, followed for $\epsilon \neq 1$ by a transition at larger Ma to a succession of $m=2$ states. At yet larger values of Ma (not shown), one finds a pair of transitions to $m=1$ states as well.

In the next set of figures, we examine the resulting behavior in the nonlinear regime. Figure 12 shows the bifurcation diagram for $\epsilon=1$ with high resolution to minimize the effects of the computational grid. The primary bifurcation at T_0 ($Ma_{T_0}=96.19$) is transcritical and produces a stable $m=0$ branch of states with fluid descending in the center and

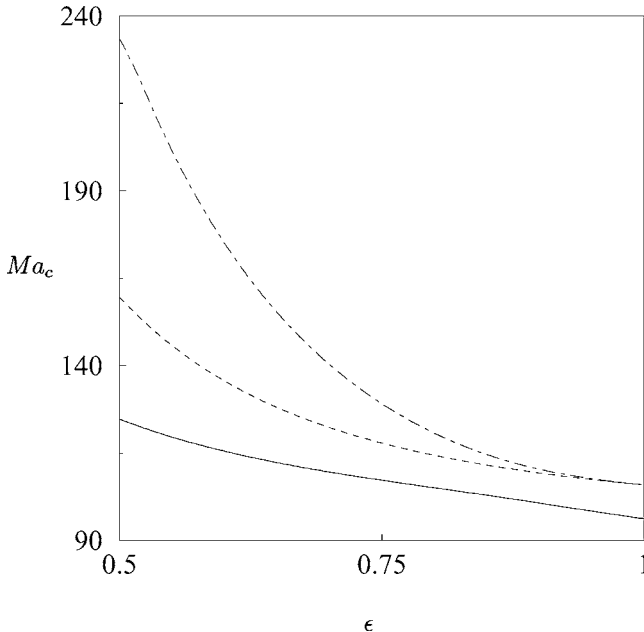


FIG. 11. Critical Marangoni number Ma_c as a function of the ellipticity ϵ . The continuous line refers to $Ma_c(T_0)$, the dashed line to $Ma_c(P_2')$, and the dot-dashed line to $Ma_c(T_2')$. Parameters are $A=1.5$ and $Pr=1$. Resolution is $N_e=12$, $n_x=n_y=n_z=10$.

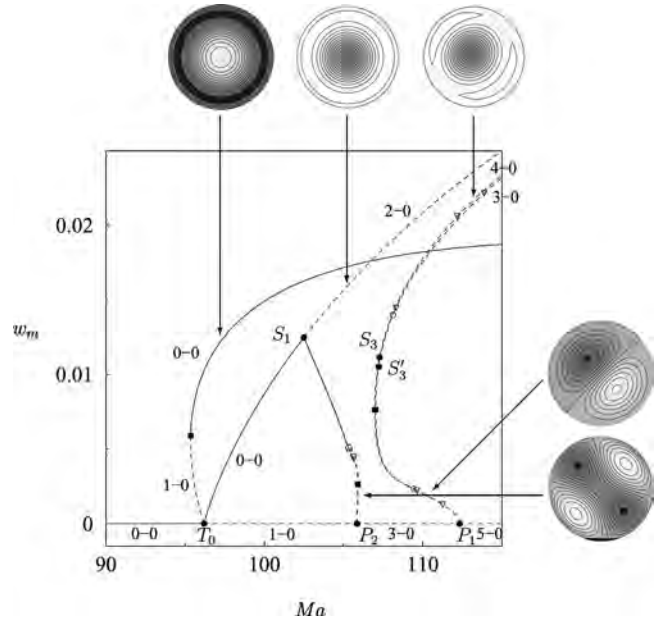


FIG. 12. Bifurcation diagram showing the maximum of the vertical velocity w_m as a function of the Marangoni number Ma . Snapshots show isovalues of the vertical velocity in the midplane of the cylinder. The orientation of the $m \neq 0$ states is nominally arbitrary. Parameters are $\epsilon=1$, $A=1.5$, and $Pr=1$. Resolution is $N_e=12$, $n_x=n_y=n_z=10$.

an unstable branch of states with ascending fluid in the center. The latter turns around at a saddle-node bifurcation (indicated by a solid square) and acquires stability, remaining stable at larger values of Ma . In addition, a branch of $m=2$ states bifurcates from the conduction state in a pitchfork of revolution at P_2 ($Ma_{P_2}=105.87$) and does so supercritically. The resulting states are once unstable near onset, but become twice unstable above a saddle-node bifurcation (indicated by a solid square), before stabilizing via a (subcritical) Hopf bifurcation. As a result, the $m=2$ branch acquires stability before its termination on the (supercritical) $m=0$ branch at S_1 . This bifurcation is again a pitchfork of revolution and destabilizes the $m=0$ states at larger values of Ma ; for future reference, we emphasize that these states have a pair of unstable eigenvalues and are hyperbolic, i.e., none of the eigenvalues along this branch are close to zero and hence subject to qualitative change under small perturbation, such as the introduction of nonzero ellipticity. It follows that at large Ma , the only stable states are the axisymmetric states with ascending fluid in the center, as expected on physical grounds. Finally, at $Ma_{P_1}=112.35$ the conduction state loses stability to solutions with $m=1$. The resulting pitchfork of revolution is subcritical, implying that the $m=1$ states are initially four times unstable. Figure 12 shows, however, that despite the high resolution used, some effects of the computational grid remain. These are most noticeable in the splitting of the $m=1$ branch emanating from P_1 , and in the presence of the bifurcation points S_3 and S_3' . These effects will be discussed in greater detail in the following section.

Figure 13 shows the corresponding bifurcation diagram for $\epsilon=0.98$. We see a dramatic effect: the primary pitchforks of revolution are both split, P_2 into a pitchfork P_2' to Π -like states and a transcritical bifurcation T_2' to κ_x -symmetric

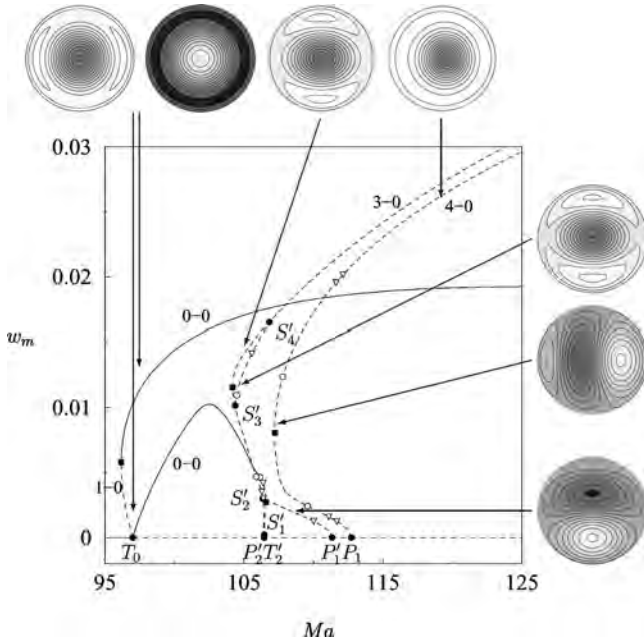


FIG. 13. Bifurcation diagram showing the maximum of the vertical velocity w_m as a function of the Marangoni number Ma . Snapshots show isovals of the vertical velocity in the midplane of the cylinder. Parameters are $\epsilon=0.98$, $A=1.5$, and $Pr=1$. Resolution is $N_e=12$, $n_x=n_y=n_z=10$.

states [Fig. 14(a)], and P_1 into a pair of pitchfork bifurcations producing κ_y -symmetric states (P'_1) and κ_x -symmetric states (P_1), respectively [Fig. 14(d)]. At the same time, the primary bifurcation (labeled T_0) remains transcritical, although the states that are produced are now D_2 -symmetric and not axisymmetric. In addition, the secondary bifurcation at S_1 is “unfolded” with the result that the supercritical branch originating at T_0 now connects to the supercritical branch emanating from T'_2 , while the subcritical branch at T'_2 connects to the large-amplitude unstable $m=0$ -like state.

As in the $A=1$ case, the unstable Π -like states rotate through 45° [Fig. 14(a)] along the branch before the branch terminates on the doubly unstable supercritical part of the transcritical branch at a point labeled S'_1 , below a saddle-node bifurcation at which the branch turns around toward smaller values of Ma [Fig. 14(c)]. At the termination, the number of unstable eigenvalues on the transcritical branch decreases to one, but at the saddle node it increases back to two, before a Hopf bifurcation stabilizes the branch. Alternatively, viewed from the perspective of the supercritical branch produced at T_0 , the solutions with descending fluid in the center lose stability with increasing Ma at a Hopf bifurcation [Fig. 14(c)]. However, no stable oscillations have been found in the vicinity of this bifurcation, suggesting that this bifurcation remains subcritical. In contrast, the subcritical part of the transcritical branch T'_2 remains unstable throughout, and is *three times* unstable at large values of Ma [Fig. 14(b)]. The branch of κ_y -symmetric states emerging from P'_1 now terminates at S'_2 on the subcritical branch created at T'_2 . In addition, there is a second segment of κ_y -symmetric states that extends from S'_3 to S'_4 and brackets the saddle node on the branch of subcritical D_2 -symmetric states emerging from T'_2 . In contrast, the branch of κ_x -symmetric states emerging

from P_1 turns around at a saddle node and extends to larger values of Ma , where it is ultimately four times unstable [Fig. 14(d)]. A pair of Hopf bifurcations brackets the saddle node but the associated oscillations are necessarily unstable. Despite this, *stable* periodic oscillations are found near the saddle node in the interval $107.24 < Ma < 107.26$, between the saddle-node bifurcation and the Hopf bifurcations. These oscillations grow in amplitude with increasing Ma (Fig. 15) and are κ_x -symmetric (Fig. 16), i.e., they share the symmetry of the steady states on the branch emanating from P_1 , but their relation to this branch remains unclear.

The bifurcation diagram shown in Fig. 13 possesses two unexpected features. First, the stability assignments indicate that the two large-amplitude branches have three and four unstable eigenvalues, respectively. In contrast, the $m=0$ branch in Fig. 12 is only twice unstable, and for small perturbations of the domain this stability assignment should be inherited by the corresponding D_2 branch in Fig. 13. In addition, we expect the presence of a third branch at large Ma , since the deformation of the domain is expected to split the $m=1$ branch into two distinct branches. To reconcile Fig. 13 with Fig. 12, we have therefore recomputed the bifurcation diagram for $\epsilon=0.995$ (Fig. 17). The figure confirms that our expectation is correct, and indicates that $\epsilon=0.98$ is in fact a *large* perturbation. Indeed, as ϵ decreases, the branch of κ_y -symmetric states collides with the branch of D_2 -symmetric states, and breaks into two segments. The first of these terminates at S'_2 [Fig. 14(c)] while the second extends between S'_3 and S'_4 [Fig. 14(b)]. Evidently, as ϵ decreases, the bifurcation point S'_4 moves in from large amplitudes and is responsible for the unexpected stability properties of the D_2 -symmetric states at these amplitudes, as well as for the absence of the third large-amplitude branch. Finally, Fig. 17 also reveals the presence of a pair of Hopf bifurcations on each of the branches bifurcating from P_1 and P'_1 , each of which brackets a saddle node. The presence of these bifurcations provides strong evidence for the presence of the corresponding bifurcations in the $\epsilon=1$ case in the infinite resolution limit. In addition, the Hopf bifurcations on both of the branches bifurcating from T'_2 converge to the corresponding Hopf bifurcation in the $\epsilon=1$ case (Fig. 12).

C. Effects of the numerical grid

In this section, we examine the effects of the numerical grid noticed already in Fig. 12. For this purpose, we decrease the resolution to $n_x=n_y=6$. Figure 18 for $A=1$ shows that the grid splits the primary bifurcation P_2 to $m=2$ states into two successive bifurcations even when $\epsilon=1$. Associated with this splitting is the splitting of the termination point S_2 ; moreover, both branches inherit the Hopf bifurcation present in Fig. 3. In contrast, the primary bifurcation P_1 is not split by the grid, although the branches that emanate from it are. This branch splitting is responsible for the transfer of stability at finite amplitude between these two branches; this transfer occurs via a secondary branch of mixed states [Fig. 18(c)] and is a consequence of the fact that the $m=1$ states have a zero eigenvalue, associated with rotations, when $\epsilon=1$. Figure 19 shows the corresponding results using the total kinetic

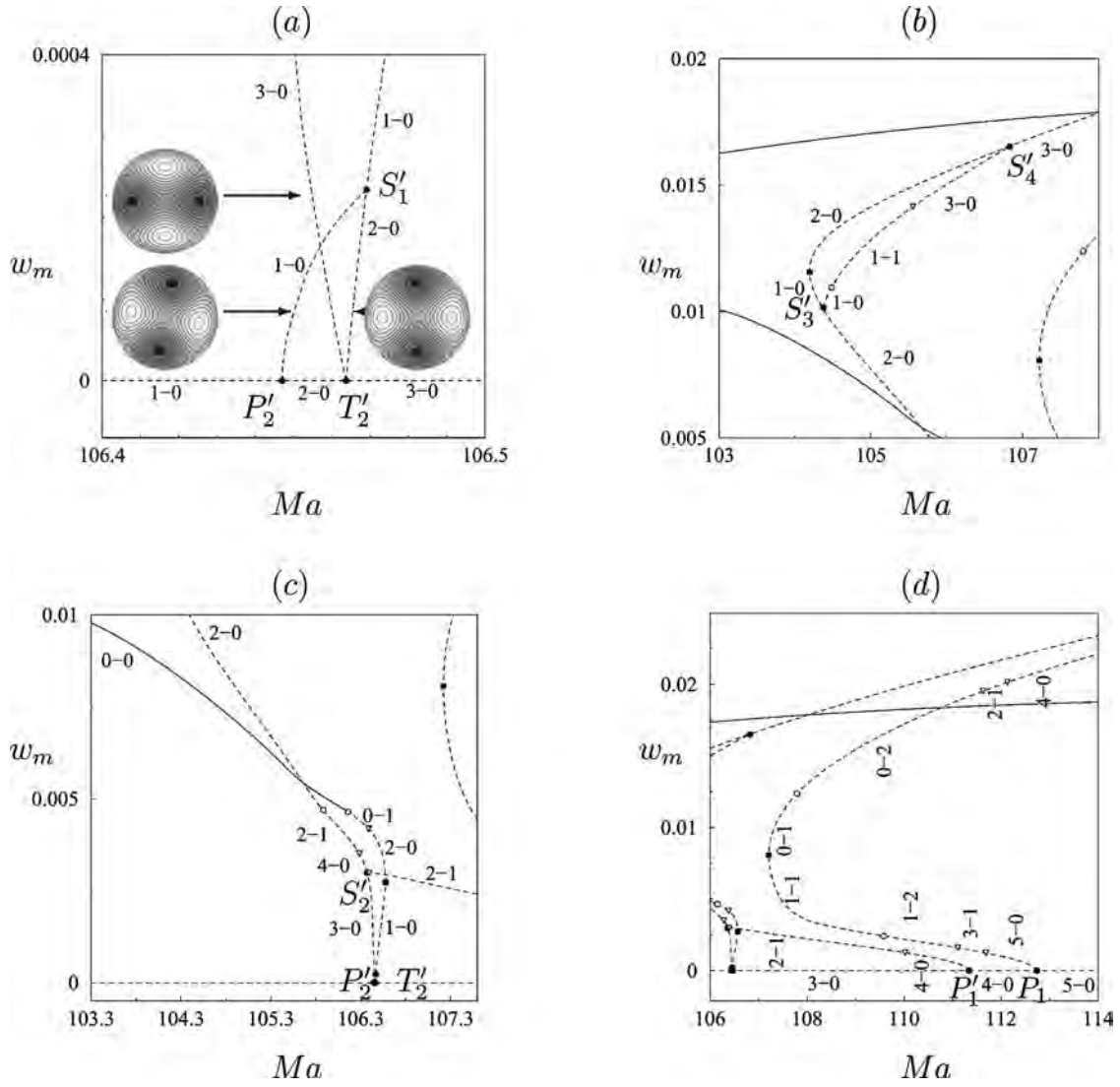


FIG. 14. Closer view of Fig. 13. Parameters are $\epsilon=0.98$, $A=1.5$, and $\text{Pr}=1$. Resolution is $N_c=12$, $n_x=n_y=n_z=10$.

energy \mathcal{E} as a measure of the solution amplitude. This procedure confirms that the splitting is due to the symmetry of the grid, and not an artefact produced by changes in the location of the maximum of $|w|$ with respect to a collocation point.

Figure 20 shows a blowup of some of the branches in Fig. 12, and demonstrates the effect of the computational grid even with the $10 \times 10 \times 10$ resolution. The figure shows that the pitchfork at P_2 is split by the grid into two nearby (pitchfork) bifurcations (P_2, P'_2), one of which is to states with κ_x symmetry and the other is to states with Π symmetry. Both branches that result undergo the same sequence of bifurcations, and these converge on the corresponding bifurcations in the nominally infinite resolution limit. In contrast, the bifurcation P_1 is not split, although two distinct solution branches emerge from it at finite amplitude. Moreover, Figs. 20(a) and 20(b) reveal the presence of one secondary Hopf bifurcation (open circle) on each branch, but this time at quite different locations. Thus the grid has a different effect on different bifurcations. As a result, the stability assignments along the split branches depend on which branch is

considered, and care must be taken when using these types of numerical results to establish stability properties in the nominally infinite resolution limit.

The effect is magnified at lower resolution, as revealed in Figs. 21–23. Note in particular the proliferation of secondary Hopf bifurcations (open circles) on the $m=1$ branches [Figs. 22(b) and 22(c)]. In contrast, the saddle-node bifurcations (solid squares) and the secondary bifurcations S_3 and S'_3 at which the branches exchange stability [Fig. 22(d)] remain almost unchanged. The new Hopf bifurcations are responsible for the presence of a narrow interval of stability above the leftmost saddle node [Fig. 22(d)]. Evidently, this interval of stability is an artefact of the low resolution, and only the bifurcations that also appear in Fig. 20 are “real.” In contrast, the bifurcations along the $m=2$ branches emanating from P_2 and P'_2 continue to track each other well (Fig. 23), although we can now discern the presence of a pair of secondary bifurcations S_2 and S'_2 at which these branches trade stability prior to their termination at S_1 and S'_1 , respectively [Fig. 23(b)].

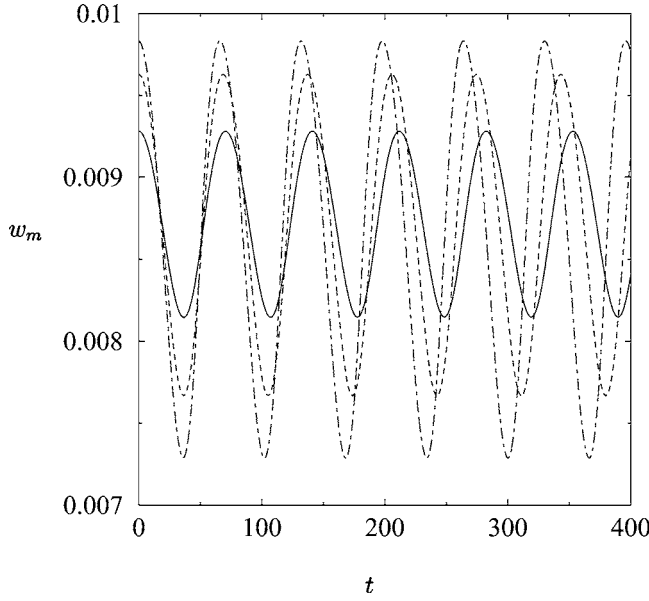


FIG. 15. Oscillations in the maximum vertical velocity w_m as a function of time obtained at $Ma=107.24$ (solid line), $Ma=107.25$ (dashed line), and $Ma=107.26$ (dot-dashed line). Parameters are $\epsilon=0.98$, $A=1.5$, and $Pr=1$. Resolution is $N_e=12$, $n_x=n_y=n_z=10$.

Figure 22 demonstrates that because of the grid, the $m=1$ branch is already split into a *pair* of hyperbolic branches, and one expects, therefore, to find three branches at large amplitude, at least for sufficiently small ellipticity; for larger ϵ , the first of the $m=1$ branches collides with and eliminates the large-amplitude $m=0$ branch, resulting in the presence at large amplitude of only two branches, one with three unstable eigenvalues and the other with four.

Once $\epsilon \neq 1$, it is the ellipticity that splits the various branches, and the grid structure plays only a minor, quantitative role. In the following section, we provide a theoretical explanation of these results.

IV. THEORETICAL DESCRIPTION

Simulations in an $A=1$ circular cylinder reveal successive bifurcations to $m=1$, 2, and 0 states; at the $m=1$, $m=2$ bifurcations, two eigenvalues become positive simultaneously, while at $m=0$ only a single eigenvalue changes sign. The simulations also reveal that in the nonlinear regime the

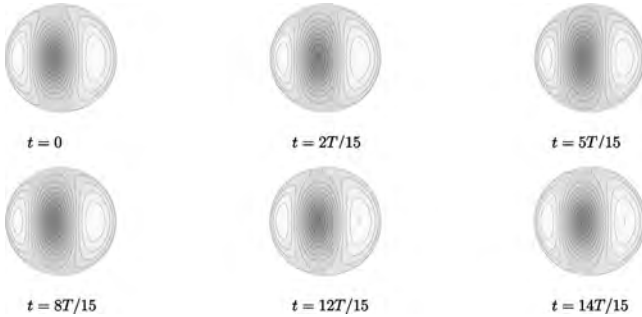


FIG. 16. Snapshots of the oscillation present at $Ma=107.25$ at six instants within one period. The oscillation is periodic and κ_x -symmetric. Parameters are $\epsilon=0.98$, $A=1.5$, and $Pr=1$. Resolution is $N_e=12$, $n_x=n_y=n_z=10$.

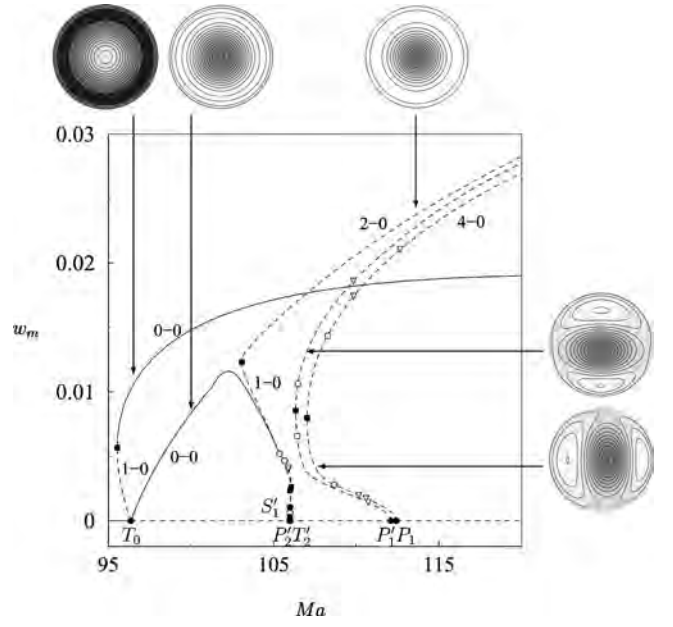


FIG. 17. Bifurcation diagram showing the maximum of the vertical velocity w_m as a function of the Marangoni number Ma . Snapshots show isovalues of the vertical velocity in the midplane of the cylinder. Parameters are $\epsilon=0.995$, $A=1.5$, and $Pr=1$. Resolution is $N_e=12$, $n_x=n_y=n_z=10$.

$m=0$ and $m=2$ states interact. These states interact in the $A=1.5$ case as well. To describe this (codimension-2) interaction, we write

$$w(r, \theta, z) = \text{Re}\{a(t)f(r, z)\exp 2i\theta\} + b(t)g(r, z) + \dots, \quad (7)$$

where w is the vertical velocity at the point (r, θ, z) , and we suppose that both modes set in in close succession, so that any interaction occurs already at small amplitude. In a cylindrical container, the equations for the amplitudes a (complex) and b (real) must commute with the following representation^{20,21} of the symmetry group $O(2)$ of rotations and reflections of a circle:

$$(a, b) \rightarrow (ae^{2i\phi}, b), \quad (a, b) \rightarrow (\bar{a}, b), \quad (8)$$

corresponding to rotations through an arbitrary angle ϕ and reflection in the x axis. Thus

$$\dot{a} = \mu a - |a|^2 a + \alpha_1 a b + \alpha_2 a b^2 + \dots, \quad (9)$$

$$\dot{b} = \nu b + \beta |a|^2 + \gamma b^2 + \dots, \quad (10)$$

where μ and ν are bifurcation parameters, and α_1 , α_2 , β , and γ are real coefficients, cf. Ref. 11. In writing these equations, we have chosen the cubic term to be stabilizing. There are two types of solutions:

$(a, b) = (0, b)$, corresponding to axisymmetric states; these bifurcate transcrically at $\nu=0$.

(a, b) , $ab \neq 0$, corresponding to $m=2$ modes; these bifurcate in a pitchfork of revolution at $\mu=0$, and are accompanied by a nonzero value of b , i.e., these solutions are *not* symmetric with respect to $w \rightarrow -w$, as observed in the simulations. As already mentioned, this is a consequence of the different boundary conditions at the top and bottom.

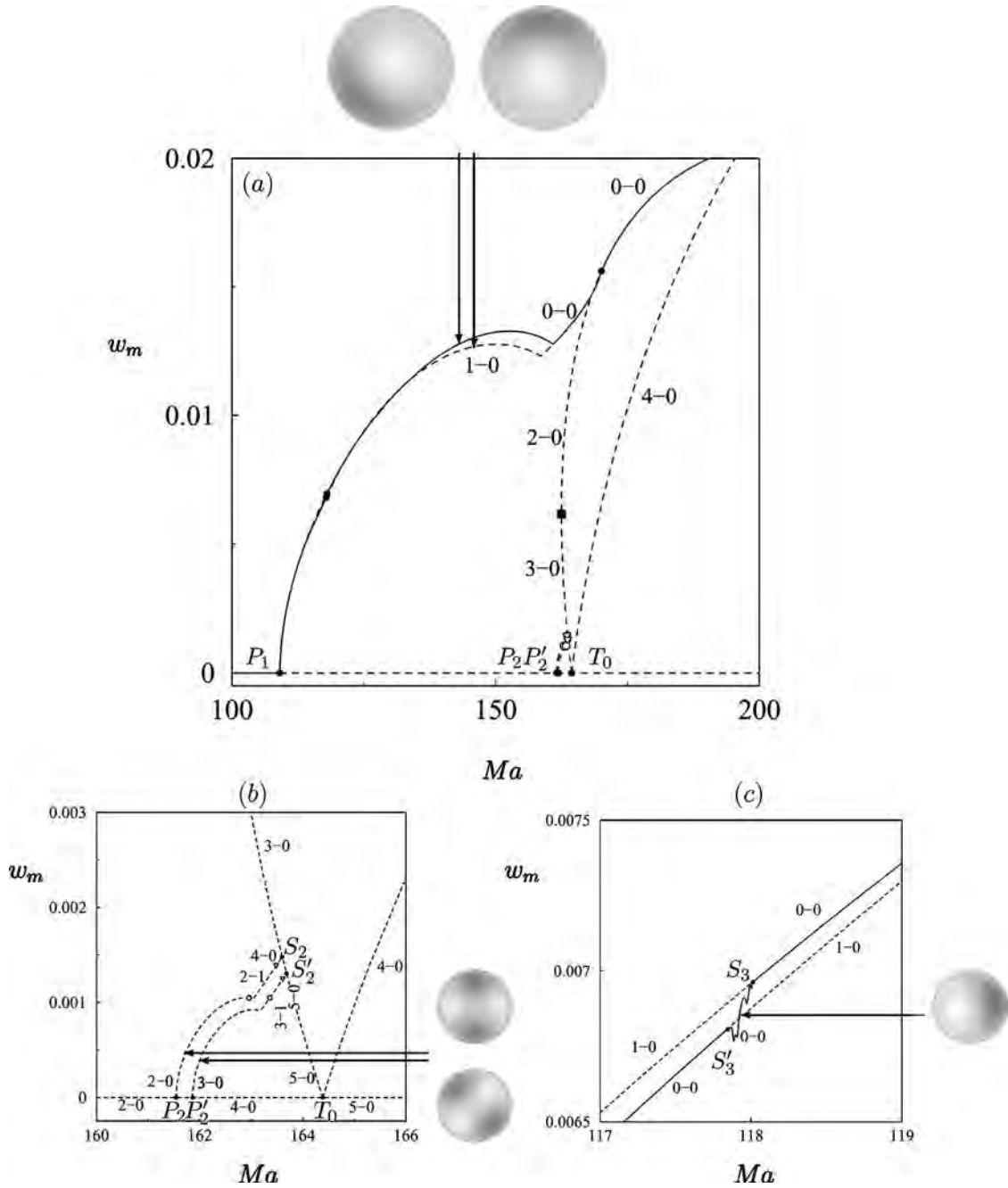


FIG. 18. (a) Bifurcation diagram showing the maximum of the vertical velocity w_m as a function of the Marangoni number Ma . Snapshots show isovalues of the vertical velocity in the midplane of the cylinder. (b),(c) Closer view of (a). Parameters are $\epsilon=1$, $A=1$, and $Pr=1$. Resolution is $N_c=12$, $n_x=n_y=6$, and $n_z=10$.

The $m=2$ branch terminates on the branch of axisymmetric states when $\mu + \alpha_1 b + \alpha_2 b^2 = 0$; this bifurcation is also a pitchfork of revolution.

A similar set of equations can be written down for the $m=1$ states. These are also accompanied by a nonzero contribution from the axisymmetric state.

A. Grid effect in a circular domain

We now explore the effect of the D_4 symmetry of the computational grid. We do so by adding to the above equations small terms that preserve the symmetry of the system under reflection in both the x and y axes, as well as in the

diagonals, but break rotational invariance. To this end we look at the bifurcations to $m=2$ and $m=1$ separately.

When $m=2$, the breaking of $O(2)$ down to D_4 symmetry leads to an equation of the form

$$\dot{a} = \mu a - |a|^2 a + \alpha_1 a b + \alpha_2 a b^2 + \dots + \epsilon \bar{a}, \quad (11)$$

where $\epsilon \ll 1$ and is real. A small term proportional to b can be added to the b equation as well. It follows that the $m=2$ mode now sets in at $\mu = \pm \epsilon$ instead of $\mu = 0$, in other words, that the primary bifurcation has been split into two successive bifurcations. The solution that sets in at $\mu = -\epsilon$ corresponds to real a and hence to states of the form w

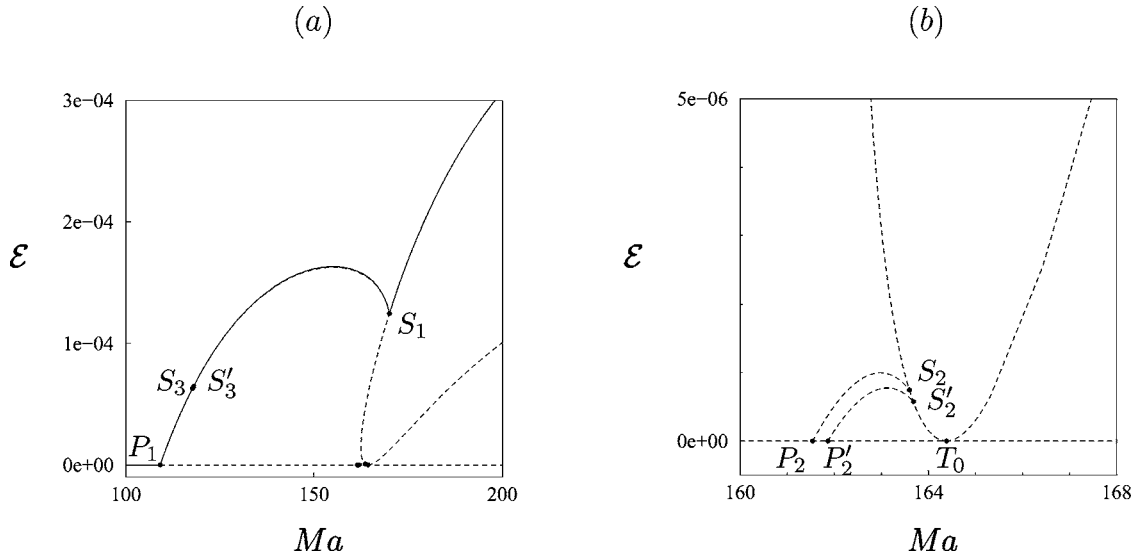


FIG. 19. (a) Bifurcation diagram showing the kinetic energy $\mathcal{E} \equiv \int_{\Omega} (u^2 + v^2 + w^2) d\Omega$ as a function of the Marangoni number Ma . (b) Closer view of (a). Parameters are $\epsilon=1$, $A=1$, and $Pr=1$. Resolution is $N_e=12$, $n_x=n_y=6$, and $n_z=10$.

$= a \cos 2\theta f(r, z) + \dots$ which are invariant with respect to reflections in the x and y axes. In contrast, the solution that sets in at $\mu = \epsilon$ corresponds to purely imaginary a and hence to states of the form $w = |a| f(r, z) \sin 2\theta + \dots$ that are invariant under reflections in the diagonals. We identify the former with the κ_x -symmetric states, and the latter with the Π -symmetric states.

In contrast, when $m=1$, the requirement that rotation by 90° leaves the system invariant (i.e., $a \rightarrow ia$) shows that the only linear term in a that can be added to Eq. (9) is proportional to a itself. Consequently, the grid does not split the bifurcation to $m=1$ states, although it may shift its location. At finite amplitude we have

$$\dot{a} = \mu a - |a|^2 a + \alpha_1 a b + \alpha_2 a b^2 + \dots + \epsilon \bar{a}^3, \quad (12)$$

where ϵ is again real. Writing $a = \rho \exp i\psi$ leads to the conclusion that $\psi=0$ or $\psi=\pi/4$, indicating the presence of two distinct branches at finite amplitude given by $\rho^2 = \tilde{\mu}(1 \pm \epsilon)$, where $\tilde{\mu} \equiv \mu + \alpha_1 b + \alpha_2 b^2$ and the \pm signs correspond to $\psi=0$ and $\psi=\pi/4$, respectively. The former are reflection-symmetric with respect to κ_x , the latter with respect to Π . Moreover, the $\psi=0$ ($\psi=\pi/4$) is stable (unstable) when $\epsilon > 0$ and vice versa. These stability assignments are modified in the obvious fashion when the bifurcation is subcritical or there are additional unstable eigenvalues that are inherited from the $a=0$ state.

B. Elliptical domain

We suppose that the cylinder is distorted into an ellipse, and that this distortion is small. This distortion preserves the conduction state $a=b=0$ but breaks the $O(2)$ symmetry down to D_2 , the symmetry of a rectangle. The symmetry is generated by reflections in the x and y axes. In addition, we include the symmetry breaking due to the grid. As already mentioned, the grid has symmetry D_4 and thus breaks the rotational symmetry of the system in a different way. In the following, it is important that the symmetries of the ellipse

are also symmetries of the grid. To incorporate both of these symmetry-breaking effects, we add to Eqs. (9) and (10) the largest terms that break the $O(2)$ symmetry in the required fashion, while preserving invariance under reflection in the x and y axes. The results depend on the azimuthal wavenumber m .

We begin with the interaction between the $m=1$ and $m=0$ modes. In this case, the symmetry $x \rightarrow -x$ acts by $(a, b) \rightarrow (-\bar{a}, b)$, while $y \rightarrow -y$ acts by $(a, b) \rightarrow (\bar{a}, b)$. It follows that

$$\dot{a} = \mu a - |a|^2 a + \alpha_1 a b + \alpha_2 a b^2 + \dots + \epsilon \bar{a}^3 + \delta \bar{a}, \quad (13)$$

$$\dot{b} = \nu b + \beta |a|^2 + \gamma b^2 + \dots, \quad (14)$$

where $\delta \ll 1$ measures the ellipticity of the container, and is real. The resulting linearized equations are uncoupled: κ_x -symmetric states bifurcate from $(0, 0)$ at $\mu = -\delta$, while κ_y -symmetric states come in at $\mu = \delta$. Weakly nonlinear analysis near each of these bifurcation points shows that these bifurcations are pitchforks. The analysis confirms the results of numerical continuation in the vicinity of the bifurcation to the $m=1$ state in both $A=1$ and 1.5 cylinders (compare Fig. 3 with Fig. 5, and Fig. 12 with Fig. 13).

We next turn to the interaction of the $m=2$ and $m=0$ modes. This time both $x \rightarrow -x$ and $y \rightarrow -y$ act by $(a, b) \rightarrow (\bar{a}, b)$, and we obtain

$$\dot{a} = \mu a - |a|^2 a + \alpha_1 a b + \alpha_2 a b^2 + \dots + (\epsilon + \delta_0) \bar{a} + \delta_1 b, \quad (15)$$

$$\dot{b} = \nu b + \beta |a|^2 + \gamma b^2 + \dots + \frac{1}{2} \delta_2 (a + \bar{a}). \quad (16)$$

In these equations, $\epsilon \ll 1$ continues to represent the effect of the grid while the $\delta_j \ll 1$ break the remaining D_4 symmetry further, down to D_2 . Note that the symmetry requirement permits the inclusion of the term $\delta_0 \bar{a}$ at linear order; thus in this case the grid effect can in effect be absorbed in the

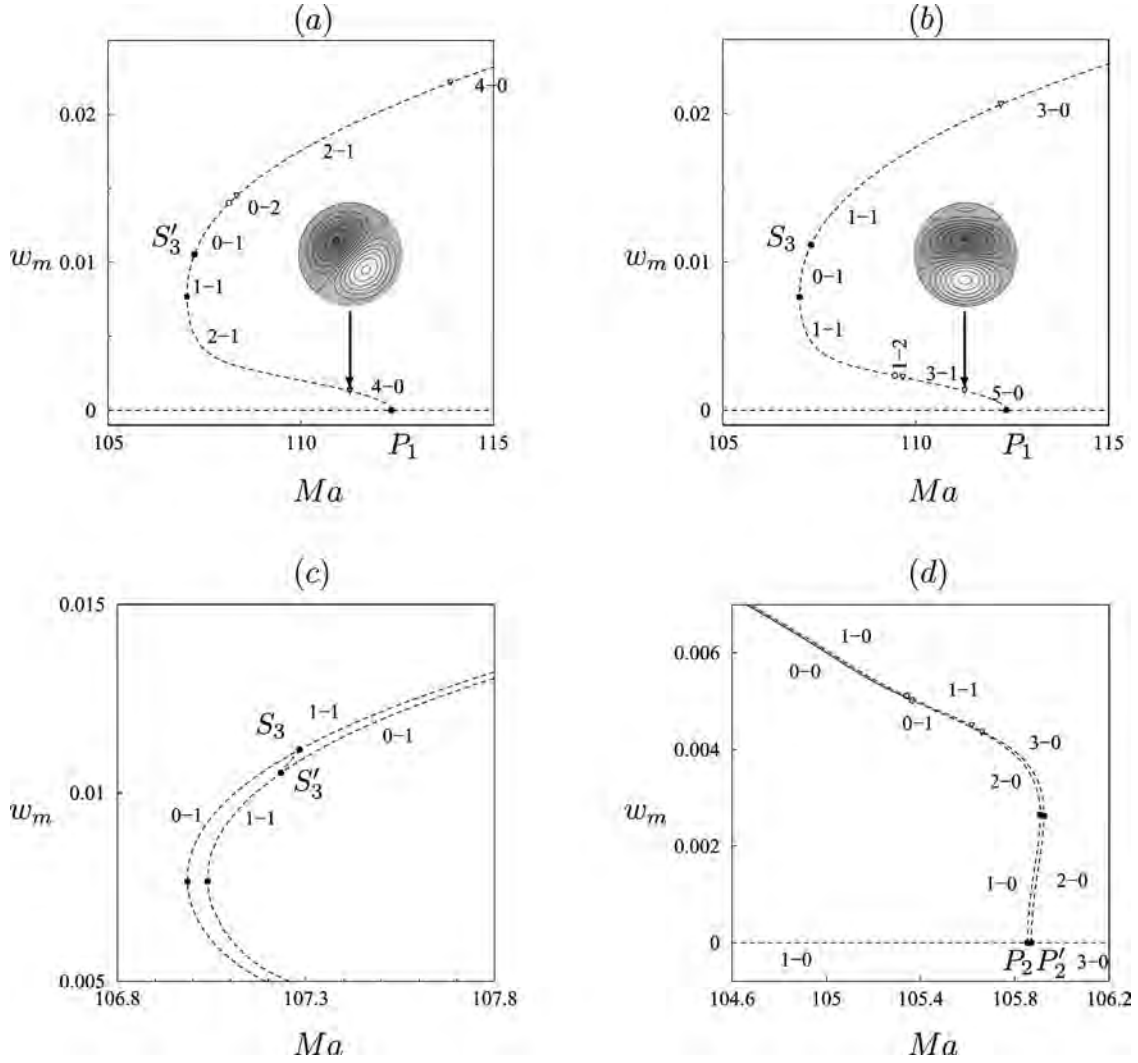


FIG. 20. Closer view of Fig. 12. (a) and (b) show the two branches of $m=1$ states due to the grid, together with their stability assignments, while (c) shows the transfer of stability between these branches. (d) shows the splitting of the $m=2$ branches emerging from P_2 , also due to the grid. In contrast to (a) and (b), the secondary Hopf bifurcations occur on both branches. Parameters are $\epsilon=1$, $A=1.5$, and $\text{Pr}=1$. Resolution is $N_e=12$, $n_x=n_y=n_z=10$.

coefficient δ_0 , although we do not choose to do so. It follows that $\epsilon \neq 0$ provides the dominant symmetry breaking effect only in circular domains.

With $a \equiv \rho \exp i\psi$ and $\varepsilon \equiv \epsilon + \delta_0$, we have

$$\mu\rho - \rho^3 + \alpha_1\rho b + \alpha_2\rho b^2 + \varepsilon\rho \cos 2\psi + \delta_1 b \cos \psi = 0, \quad (17)$$

$$\varepsilon\rho \sin 2\psi + \delta_1 b \sin \psi = 0, \quad (18)$$

$$vb + \beta\rho^2 + \gamma b^2 + \delta_2\rho \cos \psi = 0. \quad (19)$$

It follows that there are two types of solutions, satisfying $\sin \psi=0$ and $2\varepsilon\rho \cos \psi + \delta_1 b=0$, respectively. In the former case, a is real and can take either sign:

$$\mu a - a^3 + \alpha_1 a b + \alpha_2 a b^2 + \varepsilon a + \delta_1 b = 0, \quad (20)$$

$$vb + \beta a^2 + \gamma b^2 + \delta_2 a = 0. \quad (21)$$

Reconstructing the solution (7), we find

$$w(r, \theta, z) = af(r, z)\cos 2\theta + bg(r, z) + \dots \quad (22)$$

This solution describes a solution with D_2 symmetry, i.e., with two orthogonal axes of reflection. Moreover, the $\sin \psi=0$ state sets in at

$$\mu = -\varepsilon + \frac{\delta_1 \delta_2}{\nu}, \quad (23)$$

representing the threshold shift due to both the grid and the elliptical distortion. A weakly nonlinear calculation near this point shows that

$$\mu = -\varepsilon + \frac{\delta_1 \delta_2}{\nu} + \left[\frac{\alpha_1 \delta_2}{\nu} + \frac{\beta \delta_1}{\nu} + \frac{\delta_1 \delta_2^2 \gamma}{\nu^3} \right] \rho + \dots, \quad (24)$$

indicating that this bifurcation becomes *transcritical* once the circular domain is distorted ($\delta_1 \neq 0$ and/or $\delta_2 \neq 0$).

We examine next the bifurcation to the $\sin \psi \neq 0$ branch. Since

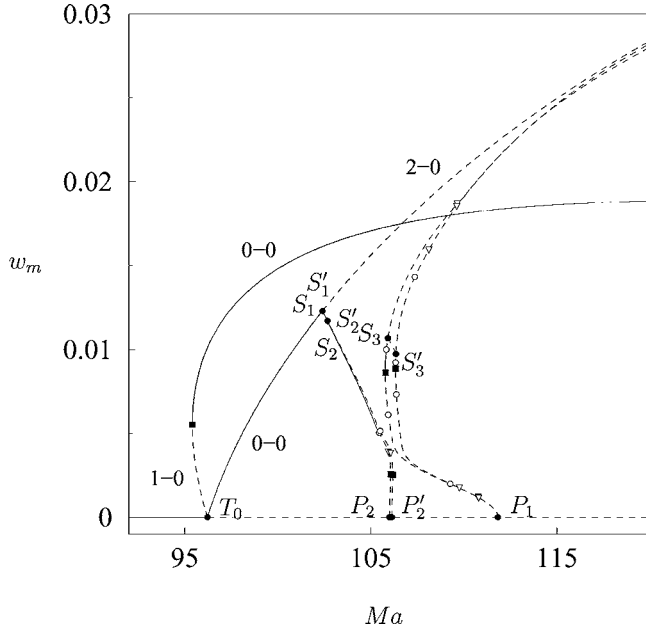


FIG. 21. Bifurcation diagram showing the maximum of the vertical velocity w_m as a function of the Marangoni number Ma . Parameters are $\epsilon=1$, $A=1.5$, and $Pr=1$. Resolution is $N_e=12$, $n_x=n_y=6$, and $n_z=10$.

$$\cos \psi = -\frac{\delta_1 b}{2\epsilon\rho} \quad (25)$$

the angle ψ will vary along the branch as a consequence of the variation of the amplitude ratio b/ρ with the bifurcation parameter μ . Equations (17) and (19) become

$$\mu - \epsilon - \rho^2 + \alpha_1 b + \alpha_2 b^2 = 0, \quad (26)$$

$$\nu b + \beta\rho^2 + \gamma b^2 - \frac{\delta_1 \delta_2 b}{2\epsilon} = 0, \quad (27)$$

implying that

$$\mu = \epsilon + \left(-\nu - \beta\alpha_1 + \frac{\delta_1 \delta_2}{2\epsilon} \right) \frac{b}{\beta} + O(b^2), \quad (28)$$

$$\rho^2 = \left(-\nu + \frac{\delta_1 \delta_2}{2\epsilon} \right) \frac{b}{\beta} + O(b^2). \quad (29)$$

The bifurcation at $\mu=\epsilon$ is therefore a pitchfork: $\rho \sim (\mu-\epsilon)^{1/2}$. Equation (25) now shows that $\cos \psi$ vanishes ($\psi \rightarrow \pi/2$) as $\mu \rightarrow \epsilon$, while $\cos \psi \rightarrow 1$ ($\psi \rightarrow 0, \pi$) as μ increases. Consequently, the spatial phase $\psi/2$ of the pattern gradually rotates with increasing supercriticality, and the total amount of rotation from the primary bifurcation to the end of the branch is $\pm\pi/4$ as found in the numerical simulations. This rotation is evidently a consequence of the interaction between the $m=2$ and $m=0$ modes, and is present whenever $(\epsilon + \delta_0)\delta_1 \neq 0$, however small, a situation that we expect to be satisfied generically in elliptically distorted domains; the simulations show that the phase rotation persists even when the corresponding primary bifurcations are far apart, and the codimension-2 analysis just described no longer applies.

The bifurcation from the axisymmetric state to $m=2$ at S_1 (Fig. 12) is of the same type as P_1 . As a result, the effect of the grid is described by

$$\dot{a} = \mu a - |a|^2 a + \dots + \epsilon \bar{a}. \quad (30)$$

There are two types of solutions, with a real or pure imaginary; these set in at $\mu = \mp \epsilon$, respectively, and correspond to states with κ_x and Π symmetry, as observed in Fig. 23. Likewise, in the absence of the grid, the effect of finite ellipticity is captured by the equation

$$\dot{a} = \mu a - |a|^2 a + \dots + \delta_0, \quad (31)$$

where $0 < |\delta_0| \ll 1$ is a real parameter.²² Thus a must be real, and for fixed δ_0 the equilibria satisfy a cubic equation. One branch grows monotonically from negative to positive μ and is stable throughout; two other (disconnected) solutions appear via a saddle node and are present in $\mu > 3(\delta_0/2)^{2/3}$ only. Both are *unstable*. These predictions agree exactly with the results shown in Fig. 17 near S_1 ; evidently, the ellipticity in this figure overwhelms the effect of the grid responsible for the splitting of the $m=2$ branches. It should be observed, however, that Eq. (31) does not capture all aspects of the loss of symmetry;²² indeed, very close to S_1 a more complete “unfolding” is provided by

$$\dot{a} = \mu a - |a|^2 a + \dots + \delta_1 \bar{a} + \delta_0. \quad (32)$$

This equation shows, by analogy with our discussion of the bifurcation at P_1 , that small intervals of secondary branches with a rotating phase may also be present, and it is precisely these that are required to reconcile the splitting of the $m=2$ branch when $\epsilon=1$ into κ_x - and Π -symmetric branches (Fig. 23) with the behavior shown in Fig. 17 for $1-\epsilon \ll 1$, which shows that the solutions on either side of S_1 connect to κ_x - and κ_y -symmetric branches.

Finally, near the primary bifurcation T_0 (i.e., $\nu=0$), we find that

$$\nu = \frac{\delta_1 \delta_2}{\mu + \epsilon} + \left[-\gamma - \frac{\delta_1 \delta_2 \alpha_1}{(\mu + \epsilon)^2} - \frac{\delta_1^2 \beta}{(\mu + \epsilon)^2} \right] b + \dots, \quad (33)$$

showing that the bifurcation to the analogue of the $m=0$ state *remains* transcritical. The above results are consistent with those presented in Figs. 5, 13, and 17.

V. DISCUSSION

In this paper, we have examined the effect of changing the container shape on pattern formation in Marangoni convection in small aspect ratio containers. The present study parallels an earlier investigation of the effects of changing the shape of the container from square to slightly rectangular.¹⁸ In the present case, the change of shape of the container from circular to elliptical has a similar effect, in that the finite ellipticity of the container splits multiplicity-2 eigenvalues, resulting not only in the appearance of multiple hyperbolic branches, but also of a variety of secondary bifurcations, including some responsible for “mode-jumping” at finite amplitude. Although none of the secondary Hopf bifurcations we have identified appears to be supercritical, i.e., none produces stable small-amplitude oscillations, we have

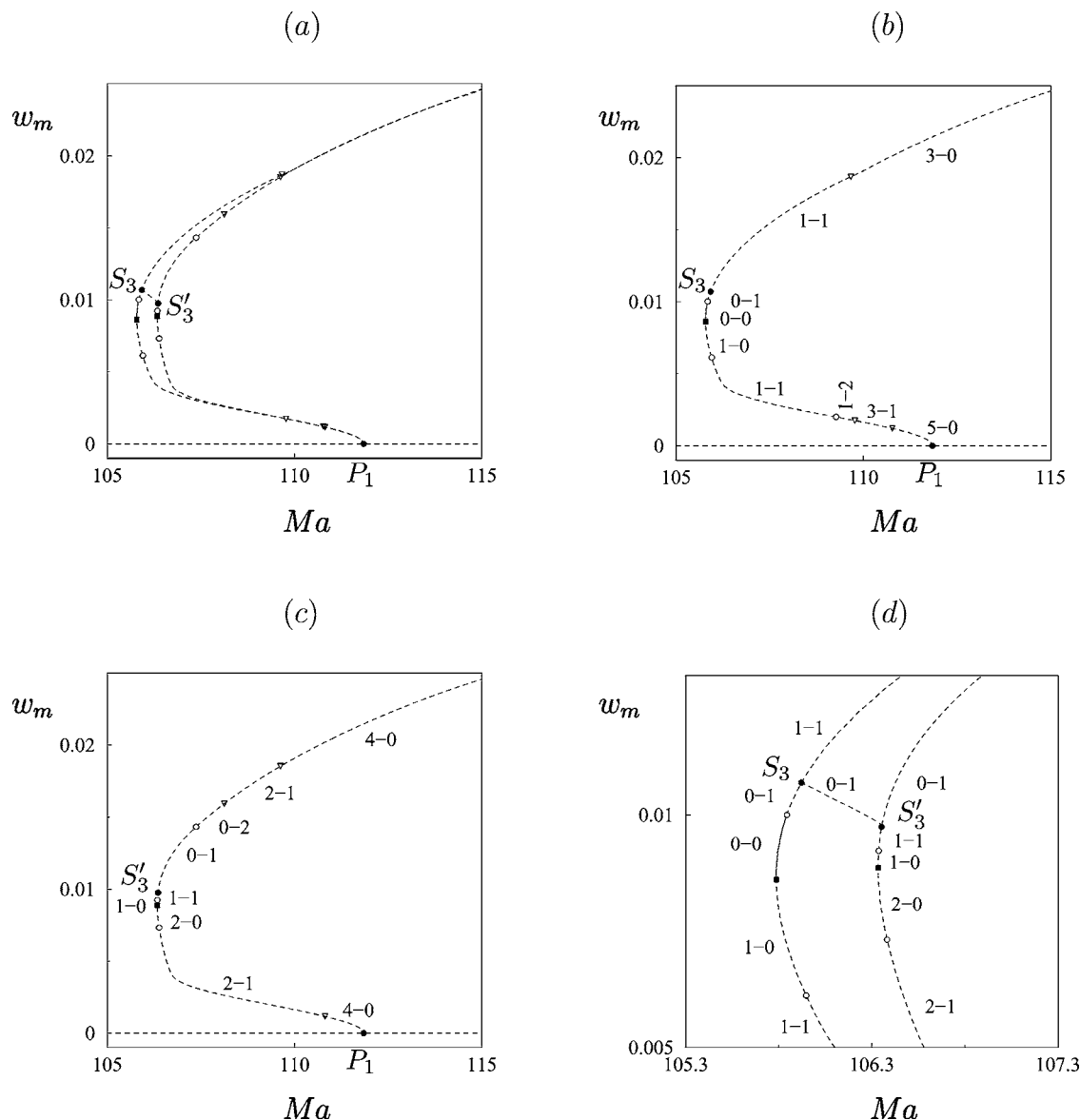


FIG. 22. (a)–(d) Closer view of Fig. 21 showing exchange of stability between the two branches emerging from P_1 . Parameters are $\epsilon=1$, $A=1.5$, and $Pr=1$. Resolution is $N_z=12$, $n_x=n_y=6$, and $n_z=10$.

nonetheless located stable *periodic* oscillations near the saddle-node bifurcation on the $m=1$ branch when $A=1.5$. At present, the origin of these unexpected oscillations remains unclear. However, it appears that these oscillations are not introduced by the elliptical distortion of the domain, in contrast to the (quasiperiodic) oscillations studied in Ref. 23.

For our computations, we have employed a code that could simultaneously be used to compute solutions in both circular and elliptical domains, and that could capture transitions that shift a pattern off-center even in a circular container. The numerical scheme employed is more accurate than finite-element techniques but employs a grid that possesses the symmetry D_4 . We have found, perhaps surprisingly, that the orientation of the pattern can be pinned to the grid, and that this pinning persists even as the resolution of the grid is substantially increased. We have shown that the presence of such pinning can be understood using appropriate ideas from bifurcation theory, and that these ideas could

be extended to incorporate the interaction between the grid and the ellipticity of the container. Although limited in scope, the theory was in all cases confirmed by our computations.

It is significant that for $A=1$, the mode that first becomes unstable is nonaxisymmetric; with increasing Marangoni numbers, the amplitude of this mode grows until a nonhysteretic transition to an axisymmetric state takes place. In experiments on the Rayleigh-Bénard-Marangoni problem, Koschmieder and Prah1² found that for $0.87 \leq A \leq 2.15$, the first state observed was always axisymmetric, an observation that may be reconciled with the theory by including both the presence of surface deformation that is present in the experiments and the nontrivial effect of a finite Rayleigh number, also neglected in the present paper. On the other hand, the prediction that for $A=1.5$ the primary instability will be a transcritical bifurcation to an $m=0$ mode is consistent not only with microgravity experiments⁷ but also with ground-based experiments² and the (extrapolated) results of Dauby

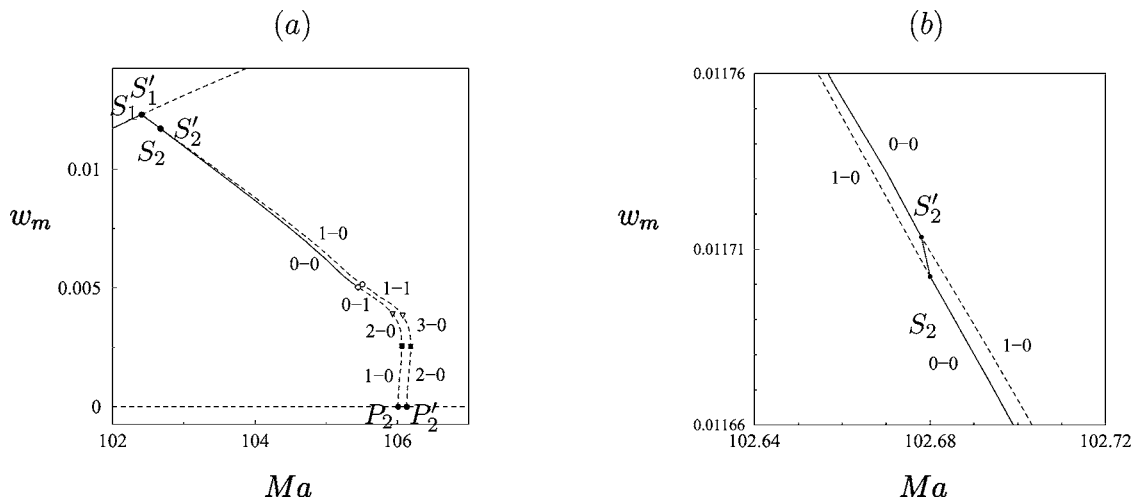


FIG. 23. (a),(b) Closer view of Fig. 21 showing exchange of stability between the two branches emerging from P_2 and P'_2 . Parameters are $\epsilon=1$, $A=1.5$, and $Pr=1$. Resolution is $N_x=12$, $n_x=n_y=6$, and $n_z=10$.

*et al.*²⁴ that do include finite Rayleigh number effects. However, with increasing aspect ratio, Dauby *et al.* predicted an onset of instability via an $m=1$ mode, followed by $m=2$ and more complex structures, while the $m=1$ state is apparently absent from Koschmieder and Prahl's experiments.

Our results suggest distinct protocols for carrying out more detailed experiments. In particular, when the primary instability is a transcritical bifurcation to an axisymmetric mode, it is vitally important to examine perturbations with both downflow and upflow in the center of the container. Specifically, our results for $A=1.5$ show that the primary instability leads to a stable $m=0$ state with downflow in the center, and that this state remains stable until a secondary bifurcation, where it acquires an $m=2$ contribution; at larger Ma this mixed state loses stability to growing oscillations, and a hysteretic transition to a stable $m=0$ state with upflow in the center takes place. This state remains stable for larger Ma . In fact, these upflow states are stable down to a saddle-node bifurcation where the system undergoes a hysteretic transition back to the conduction state. It is significant that upflow states of this type have indeed been observed under microgravity conditions.⁷ When the domain is deformed into an ellipse, the downflow $m=0$ and $m=2$ branches form a single continuous branch, but the hysteretic transition to the upflow state with increasing Ma remains. An appropriate experimental protocol focusing on downflow states near onset could in principle confirm the presence of both hysteresis loops and detect any (finite-amplitude) oscillations that may be associated with the loss of stability of the downflow state.

The results described here are largely insensitive to the precise value of the Prandtl number. In particular, for $Pr=7$, $A=1$, the global properties of the bifurcation diagrams are not drastically affected. For example, when $\epsilon=1$, the Marangoni number of the secondary bifurcation S_1 (Fig. 3) is hardly affected. When $\epsilon=0.98$, the only noticeable change occurs along the supercritical part of the branch emerging from T'_2 . Here two saddle nodes are present in succession, and the eigenvalues change from 2-0 to 3-0 and then back to 2-0, thereby recovering the stability properties indicated in

Figs. 5 and 6 prior to the connection with the branch emerging from P'_1 . An additional change occurs along the subcritical part of the branch emerging from T'_2 : the Hopf bifurcation is now absent and is replaced by two saddle-node bifurcations. We have been unable, however, to recover the oscillations observed when $Pr=1$ and $A=1.5$ (Fig. 15). This comes as no surprise since in problems of this type, a lower value of Pr favors the presence of oscillations.

It is noteworthy that we have seen no evidence of the dynamics expected to arise from the interaction of the $m=1$ and $m=2$ modes in circular containers.^{25,26} The most dramatic feature of this interaction is the presence, in certain parameter regimes, of structurally stable heteroclinic cycles connecting the $m=2$ state with its rotations by $\pi/4$. Such cycles have been observed in $A=2.5$ containers by Johnson and Narayanan⁵ and reproduced within weakly nonlinear theory by Dauby *et al.*,²⁴ see also Ref. 7. Presumably this is so because the aspect ratios we have used are too far from the required codimension-2 point for this interaction.

ACKNOWLEDGMENTS

This work was supported in part by a CNRS Projet International de Cooperation Scientifique (PICS 3471) and by the National Science Foundation under Grant No. DMS-0305968.

¹H. Bénard, "Les tourbillons cellulaires dans une nappe liquide," Rev. Gen. Sci. Pures Appl. **11**, 1261 (1900).

²E. L. Koschmieder and S. A. Prahl, "Surface-tension-driven Bénard convection in small containers," J. Fluid Mech. **215**, 571 (1990).

³T. Ondarçuhu, G. B. Mindlin, H. L. Mancini, and C. Pérez-García, "Dynamical patterns in Bénard-Marangoni convection in a square container," Phys. Rev. Lett. **70**, 3892 (1993).

⁴T. Ondarçuhu, J. Millán-Rodríguez, H. L. Mancini, A. Garcimartín, and C. Pérez-García, "Bénard-Marangoni convective patterns in small cylindrical layers," Phys. Rev. E **48**, 1051 (1993).

⁵D. Johnson and R. Narayanan, "Experimental observation of dynamic

- mode switching in interfacial-tension-driven convection near a codimension-two point,” *Phys. Rev. E* **54**, R3102 (1996).
- ⁶R. Pasquetti, P. Cerisier, and C. Le Niliot, “Laboratory and numerical investigations on Bénard-Marangoni convection in circular vessels,” *Phys. Fluids* **14**, 277 (2002).
- ⁷D. Schwabe, “Marangoni instabilities in small circular containers under microgravity,” *Exp. Fluids* **40**, 942 (2006).
- ⁸M. F. Schatz and G. P. Neitzel, “Experiments on thermocapillary instabilities,” *Annu. Rev. Fluid Mech.* **33**, 93 (2001).
- ⁹B. Hof, P. G. J. Lucas, and T. Mullin, “Flow state multiplicity in convection,” *Phys. Fluids* **11**, 2815 (1999).
- ¹⁰W. Meevasana and G. Ahlers, “Rayleigh-Bénard convection in elliptic and stadium-shaped containers,” *Phys. Rev. E* **66**, 046308 (2002).
- ¹¹S. Rosenblat, S. H. Davis, and G. M. Homsy, “Nonlinear Marangoni convection in bounded layers. Part 1. Circular cylindrical containers,” *J. Fluid Mech.* **120**, 91 (1982).
- ¹²G. Em. Karniadakis, M. Israeli, and S. A. Orszag, “High-order splitting method for the incompressible Navier-Stokes equations,” *J. Comput. Phys.* **97**, 414 (1991).
- ¹³K. Mamun and L. Tuckerman, “Asymmetry and Hopf bifurcation in spherical Couette flow,” *Phys. Fluids* **7**, 80 (1995).
- ¹⁴A. Bergeon, D. Henry, H. BenHadid, and L. S. Tuckerman, “Marangoni convection in binary mixtures with Soret effect,” *J. Fluid Mech.* **375**, 143 (1998).
- ¹⁵P. C. Dauby, G. Lebon, and E. Bouhy, “Linear Bénard-Marangoni instability in rigid circular containers,” *Phys. Rev. E* **56**, 520 (1997).
- ¹⁶H. Herrero and A. M. Mancho, “On pressure boundary conditions for thermoconvective problems,” *Int. J. Numer. Methods Fluids* **39**, 391 (2002).
- ¹⁷A. Vidal and A. Acrivos, “Nature of the neutral state in surface-tension driven convection,” *Phys. Fluids* **9**, 615 (1966).
- ¹⁸A. Bergeon, D. Henry, and E. Knobloch, “Three-dimensional Marangoni-Bénard flow in square and nearly square containers,” *Phys. Fluids* **13**, 92 (2001).
- ¹⁹C. Canuto, M. Hassani, A. Quarteroni, and T. A. Zang, *Spectral Methods in Fluid Mechanics* (Springer-Verlag, New York, 1987).
- ²⁰J. D. Crawford and E. Knobloch, “Symmetry and symmetry-breaking bifurcations in fluid dynamics,” *Annu. Rev. Fluid Mech.* **23**, 341 (1991).
- ²¹M. Golubitsky, I. Stewart, and D. G. Schaeffer, *Singularities and Groups in Bifurcation Theory* (Springer-Verlag, New York, 1988), Vol. 2.
- ²²M. Golubitsky and D. G. Schaeffer, “A discussion of symmetry and symmetry breaking,” *Proc. Symp. Pure Math.* **40**, 499 (1983).
- ²³A. Bergeon and E. Knobloch, “Oscillatory Marangoni convection in binary mixtures in square and nearly square containers,” *Phys. Fluids* **16**, 360 (2004).
- ²⁴P. C. Dauby, P. Colinet, and D. Johnson, “Theoretical analysis of a dynamic thermoconvective pattern in a circular container,” *Phys. Rev. E* **61**, 2663 (2000).
- ²⁵D. Armbruster, J. Guckenheimer, and P. Holmes, “Heteroclinic cycles and modulated travelling waves in systems with $O(2)$ symmetry,” *Physica D* **29**, 257 (1988).
- ²⁶I. Mercader, J. Prat, and E. Knobloch, “Robust heteroclinic cycles in two-dimensional Rayleigh-Bénard convection without Boussinesq symmetry,” *Int. J. Bifurcation Chaos Appl. Sci. Eng.* **12**, 2501 (2002).